Thermal boundary resistance Chapter 8
within optoelectronic devices

8.1 Introduction

The prediction of the thermal properties of modern semiconductor devices at the design stage is essential to obtain efficient heat management, ensure long lifetimes, high power operation and high reliability. With the ever increasing need for higher power devices, higher heat dissipation densities are inescapable. Indeed, it is common for heating rates as high as $5x10^{15}Wm^{-3}$ to be present in modern devices. A great deal of attention has been paid to the derivation of the heat generation terms used in device models [1-8]. However, less attention has been paid to the propagation of heat within the device itself. In particular, the thermal resistance associated with epitaxial interfaces is commonly neglected. As heat flows across an epitaxial interface, a small, but measurable, temperature step is produced due to phonon reflection. The reflection occurs because of the acoustic mismatch of the two materials (analogous to total internal reflection in optics) and the scattering of phonons off of interface defects. This temperature discontinuity can be represented as a thermal boundary resistance (TBR). The thermal boundary resistance is called Kapitza [9] resistance and is defined as "the ratio of the temperature discontinuity at the interfaces to the power per unit area flowing across it" [10]. This can be written as

$$q R = \Delta T \quad , \tag{8.1}$$

where q is the heat flux, R_B is the TBR and ΔT is the temperature drop across the

interface [3].

It has recently been shown both numerically [11] and experimentally [12],[13], that the effects of acoustic mismatch can significantly reduce heat propagation within devices [11]. Indeed, in GaAs/AlAs superlattices at room temperature, a reduction in the thermal conductivity of up to an order of magnitude from the averaged bulk thermal conductivities has been observed [13]. The scattering of phonons off of interface defects is of particular interest in dilute nitride devices due to the increased interface roughness arising from the incorporation of nitrogen [14]. If one considers the possibility of a TBR at every epitaxial interface, then the validity of applying Fourier's heat equation directly to these state-of-the-art optoelectronic should be examined more carefully [11].

8.2 Chapter outline

In this chapter, the concept of thermal boundary resistance is introduced. Theoretical models for the calculation of the TBR value are examined and the state of current knowledge is assessed. A finite difference scheme is developed, which is capable of accurately introducing a TBR and a step-wise gradient change in temperature at material interfaces in a device simulator. The impact of including TBR on structures with tens of epitaxial layers (e.g. VCSELs) is then examined. The discretisation scheme is then introduced into full 2D electro-optical-thermal simulations of edge emitting devices. Both a low power 1.3μm dilute nitride laser and a 980nm high-power ridge waveguide (RW) laser are examined. Finally, the interaction of the

carrier heat fluxes and the lattice heat fluxes passing through a TBR are examined.

8.3 The magnitude of TBR

There are three main factors which affect the magnitude of the TBR at an interface. These are the acoustic mismatch of the material interfaces, the quality of the material interface and the average layer thickness, L, relative to the phonon mean free path. If the materials that make up an interface are mechanically very similar in terms of their elastic constants and densities, then the reflection of phonons incident on the interface will be small. This is analogous to impedance matching of transmission lines in electro-magnetics [15]. An example of such a material system is GaAs/AlAs. For materials which are mechanically dissimilar, phonons will have a far higher probability of reflection at the interface. In this case, a higher TBR will be associated with the interface. An example of such a material system is GaN/sapphire.

At high temperatures, where high frequency phonons dominate the heat transport, interface scattering is very probable. Imperfections at the interface have been shown to increase the thermal boundary resistance. Indeed, it has been shown [16] that interface roughness of only a few monolayers thickness can dramatically increase the predicted value of TBR.

The average layer thickness, L, and the average phonon mean free path, Λ are also important factors [17]. In general, there are two regimes of TBR. In devices where the layer thicknesses are either comparable to the phonon mean free path ($L \approx \Lambda$) or

bigger than it, ($L>>\Lambda$), the devices can be modelled using the bulk thermal conductivities for each epitaxial layer together with a TBR at each epitaxial interface. For devices where the average phonon mean free path is greater than several layer thicknesses, $L<<\Lambda$, the phonon behaviour becomes more complex with the possibility of a phonon reflection from multiple layers before scattering. This alters the phonon density of states, which severely reduces the thermal conductivity [17]. The average mean free path in GaAs/AlGaAs is ~20nm [17,18]. Thus, the majority of standard edge-emitting lasers generally fall within the $L\approx\Lambda$ regime, but QCLs and some VCSEL mirrors do not.

8.3.1 Models for the calculation of TBR

There are three main approaches to calculating the value of the TBR. The first model to be described in the literature was the Acoustic Mismatch Model (AMM) by Little in 1959 [19,20]. In this model, it is assumed that phonons can be described by plane waves interacting with a defect free interface. Continuum mechanics is used to model the interface and calculate the phonon transmission probabilities. At low temperatures, this method has had some success [21]. The discrepancies between the AMM and experiment were often put down to the failure to include interface scattering. The Diffuse Mismatch Model (DMM) model was proposed by Swartz [10] to account for interface scattering. In this model, it is assumed that all phonons scatter at the interface. The DMM has shown more success at higher temperatures [10]. DMM only assumes elastic scattering at the interface, with no mode conversion of

phonons. Both the DMM and the AMM make no allowance for the size of the structure, i.e. they assume that there are no interactions with other interfaces [20]. The third method of calculating TBR is modelling the interface as a series of atoms connected by springs. Phonon wave packets are then propagated along the lattice across the interface and the results of the simulation examined. This is the molecular dynamics approach [20]. Other models have been developed which include electron-phonon interactions at the interface, but there is little experimental evidence to support them [20,22,23].

In conclusion, there have been various proposals made as to suitable models to calculate TBR, some of which agree with experiment under certain conditions. However, there is no consensus on a model which can reliably predict the value of TBR at an interface. This is due mainly to the difficulty of making accurate and reproducible measurements and the inability to change one variable at a time.

8.3.2 The Acoustic Mismatch Model (AMM)

It is the aim of the AMM and DMM to calculate the heat flux across a material interface whilst taking phonon reflection into account. The general method is to calculate the gross phonon flux across the interface from either side. Then, by subtracting and taking into account reflections, a value for the thermal resistance of the TBR can be arrived at. The first step is to calculate the phonon population at the interface. The 3D phonon density of states is given by

$$D(\omega)\,d\omega=\frac{4\pi}{(c\,2\pi)^3}\omega^2\,d\omega \quad , \tag{8.2}$$

where ω is the angular frequency of the phonon and *c* its velocity. A linear dispersion relation is assumed, i.e. ω=*ck*, where *k* is the wavevector. The function *N*(ω,T) can then be defined as the product of the phonon density of states and the phonon occupation probability

$$N(\omega,T)=D(\omega)\,f_{BE}(\omega,T) \quad , \tag{8.3}$$

where

$$f_{BE}(\omega)=\frac{1}{e^{\hbar\omega/kT}-1} \tag{8.4}$$

is given by the Bose-Einstein distribution. The phonon flux normal to the interface is then calculated following [19]. For side 1 of the interface, $c_1\cos\theta$ is the component of phonon velocity normal to the interface. It is assumed that the phonons are thermalised and scatter in all directions equally. The area element in spherical coordinates is given by,

$$dA=r^2\,d\phi\sin\theta\,d\theta \quad . \tag{8.5}$$

Therefore the number of phonons of angular frequency ω at temperature *T* incident on an area *dA* between angle θ_1 and $\theta_1+d\theta_1$ per unit time is given by [19],

$$\frac{\int_0^{2\pi} N_1(\omega,T)\,c_1\cos\theta_1\sin\theta_1\,d\phi\,d\theta_1\,dA}{\int_0^{2\pi}\int_0^{\pi}\sin\theta_1\,d\phi\,d\theta_1}=\frac{1}{2}N_1(\omega,T)\,c_1\cos\theta_1\sin\theta_1\,d\theta_1\,dA \quad , \tag{8.6}$$

where $\int_0^{2\pi}\int_0^{\pi}\sin\theta_1\,d\phi\,d\theta_1$ is a normalising area. The net heat flow across the

interface is therefore given as

$$Q=\frac{1}{2}\int\int\int N_1(\omega)\hbar\omega\alpha_1(\theta_1)c_1\cos\theta_1\sin(\theta_1)d\theta_1 d\omega_1 dA- \frac{1}{2}\int\int\int N_2(\omega)\hbar\omega\alpha_2(\theta_2)c_2\cos\theta_2\sin(\theta_2)d\theta_2 d\omega_2 dA \quad , \tag{8.7}$$

where α is the transition coefficient. The integral can be rearranged and simplified to

$$Q=\frac{A}{2}\int_0^{\frac{\pi}{2}}\alpha_1(\theta_1)\sin(\theta_1)d\theta_1\int_0^{\omega_D}N_1(\omega)\hbar\omega d\omega_1- \frac{A}{2}\int_0^{\frac{\pi}{2}}\alpha_2(\theta_2)\sin(\theta_2)d\theta_2\int_0^{\omega_D}N_2(\omega)\hbar\omega d\omega_2 \quad . \tag{8.8}$$

Rewriting gives,

$$Q=\frac{A}{2}\Gamma_1\int_0^{\omega_D}N_1(\omega)\hbar\omega d\omega_1-\frac{A}{2}\Gamma_2\int_0^{\omega_D}N_2(\omega)\hbar\omega d\omega_2 \quad , \tag{8.9}$$

where,

$$\Gamma=\Gamma_1=\Gamma_2=\int_0^{\frac{\pi}{2}}\alpha_1(\theta_1)\sin(\theta_1)d\theta_1=\int_0^{\frac{\pi}{2}}\alpha_2(\theta_2)\sin(\theta_2)d\theta_2 \quad . \tag{8.10}$$

The integrals in equation 8.9 represent the energy density within one phonon mode of the materials on either side of the interface. If it is assumed, as in [19], that the transition probability Γ is the same on both sides of the interface, equation 8.10 may therefore be written as

$$Q=\frac{A}{2}\Gamma\left(\int_0^{\omega_D}N_1(\omega)\hbar\omega d\omega_1-\int_0^{\omega_D}N_2(\omega)\hbar\omega d\omega_2\right) \quad . \tag{8.11}$$

Evaluation of 8.11 results in

$$Q=\frac{2\pi k^4\Gamma A}{h^3c_1^2}[T_1^4f(T_1)-T_2^4f(T_2)] \quad , \tag{8.12}$$

where

$$\Gamma = \int_0^{\frac{\pi}{2}} \alpha(\theta_1)\sin(\theta_1)\cos(\theta_1)\, d\theta_1 \quad , \tag{8.13}$$

$$f(T) = \int_0^{z_d} \frac{z^3}{e^z - 1}\, dz \quad , \tag{8.14}$$

$$z = \frac{\hbar\omega}{kT} \quad \text{and} \tag{8.15}$$

$$z_D = \frac{\hbar\omega_D}{kT} \quad . \tag{8.16}$$

The Debye frequency is taken as ω_D and z_D is often taken to be ∞ as in [19]. This is acceptable at low temperatures because $z_D \ll 1$, but it is not acceptable at high temperatures. Therefore, at high temperatures one may write

$$e^z = 1 + z \quad , \tag{8.17}$$

which after integration gives

$$f(T) = \frac{z_D^3}{3} = \left(\frac{\hbar\omega_D}{kT}\right)^3 \frac{1}{3} \quad , \tag{8.18}$$

from which ω_D must be found. As acoustic phonons are responsible for the majority of the heat transport, only the three acoustic modes will be taken into account. (Acoustic phonons have a much higher phase velocity than optical phonons.) If N atoms are considered, each with 3 degrees of freedom, the Debye frequency can be calculated from

$$\omega_D = c\sqrt[3]{\frac{6\pi^2 N}{V}} \quad , \tag{8.19}$$

where N is the number of atoms in the sample, V is the volume of the sample and c is

the phonon propagation speed. The total number of atoms in a sample is given by

$$N = \frac{\rho V A_0 b}{RAM} \quad , \tag{8.20}$$

where A_0 is Avogadro's number, RAM is the relative atomic mass (Kg/mole) of the atomic basis, b is the number of atoms in the atomic basis and is ρ the density of the substance. Substituting 8.20 into 8.19 one obtains

$$\omega_D = c \sqrt[3]{\frac{6\pi^2 A_0 \rho b}{RAM}} \quad . \tag{8.21}$$

Substituting 8.18 into 8.12 results in

$$Q = \frac{k \Gamma A}{(2\pi)^2 c_1^2 3} [T_1 \omega_{DI}^3 - T_2 \omega_{D2}^3] \quad . \tag{8.22}$$

The values of Γ can either be calculated graphically from [19] or calculated from the full solution of the tensor equations governing the behaviour of the interface [15]. When both transverse and longitudinal acoustic waves are included in 8.22, one obtains [19]

$$Q = \frac{k A}{(2\pi)^2 3} \left(\frac{\Gamma_l}{c_1^2} + \frac{2\Gamma_t}{c_t^2} \right) [T_1 \omega_{DI}^3 - T_2 \omega_{D2}^3] \quad . \tag{8.23}$$

From this equation, the heat drop across the interface can be calculated.

8.Error: Reference source not found3.3 The Diffuse Mismatch Model (DMM)

The main assumption made within the AMM theory is that continuum mechanics holds, so that there is no diffuse scattering at the interface [10]. In DMM theory, it is assumed that all phonons scatter at the interface and that continuum acoustics does not apply. In the DMM, the transition probability is determined only by the ratio of the

density of states on either side of the interface [24].

The DMM theory assumes that:

1. both sides of the interface are isotropic;
2. the transition probability is independent of temperature;
3. there are no anharmonic interactions;
4. as phonons scatter on the interface they 'forget' where they came from and
5. a phonon incident on the interface scatters immediately.

The thermal boundary resistance is given by

$$h_{Bd}=\frac{Q_{2\to1}^{gross}(T_2)-Q_{1\to2}^{gross}(T_1)}{A(T_2-T_1)} \quad . \tag{8.24}$$

As long as the densities of phonon states on both sides of the interface are relatively close and only a small temperature step (T_2-T_1) is experienced across the interface, the gross heat flux from side 2 of the interface may be approximated as the heat flux term from side 1 at temperature T_2, i.e.

$$Q_{2\to1}^{gross}(T_2)\approx Q_{1\to2}^{gross}(T_2) \quad . \tag{8.25}$$

Thus, equation 8.24 can be rewritten as

$$h_{Bd}=\frac{Q_{1\to2}^{gross}(T_2)-Q_{1\to2}^{gross}(T_1)}{A(T_2-T_1)} \quad . \tag{8.26}$$

In the DMM, the phonons 'forget' where they come from when they impact on the interface, so that the transition probability α is not dependant upon wave vector. Thus, the transition probability can be simplified so that

$$\alpha_{i,j}(\omega,\boldsymbol{k})=\alpha_i(\omega) \quad \text{[10]}. \tag{8.27}$$

A notation has been adopted here, whereby *i* donates the side of the boundary from

which the phonon came, i.e. 1 or 2, and *j* denotes the mode of the phonon. Equations 8.2-8.6 are still valid as no generalisation was made. Thus, the heat current may be written as

$$\frac{Q_{1\to 2}^{gross}(T)}{A}=\frac{1}{2}\sum_j \int_0^{\pi/2}\int_0^{\omega_1^{max}} N_{1,j}(\omega,T)\hbar\omega c_{1,j}\alpha_{1\to 2}(\theta,j,\omega)\cos\theta \sin\theta d\theta d\omega \tag{8.28}$$

The number of phonons with energy $\hbar\omega$ per unit area leaving side *i* is given by

$$\frac{1}{2}\sum_j \int_0^{\pi/2} N_{i,j}(\omega,T)c_{i,j}\alpha(j,\omega)\cos\theta \sin\theta d\theta \quad . \tag{8.29}$$

As the transition probabilities are independent of angle, the integration can be done resulting in 1/2, giving

$$\frac{1}{4}\left(\sum_j c_{i,j}N_{i,j}(\omega,T)\right)\alpha_i(\omega) \quad . \tag{8.30}$$

Using the assumptions 1-4, and also assuming that both sides of the boundary have the same Debye frequency, it can be shown [10] that the transition probability α can be written as

$$\alpha_i(\omega)=\frac{\sum_j c_{3-i,j}^{-2}}{\sum_{i,j} c_{i,j}^{-2}} \quad . \tag{8.31}$$

Equations 8.28 and 8.26 can then rewritten as

$$h_{Bd}=\frac{1}{2}\sum_j c_{1,j}\Gamma_{1,j}\int_0^{\omega_1^{Debye}} \hbar\omega\frac{dN(\omega,T)}{dT}d\omega \quad , \tag{8.32}$$

with

$$\Gamma_{1,j}=\int_0^{\pi/2}\alpha_{1\to 2}(\theta,j)\cos\theta\sin\theta\, d\theta \quad . \tag{8.33}$$

Therefore, substituting 8.31 into 8.33 and integrating gives

$$\Gamma_{i,j}(\omega)=\frac{1}{2}\frac{\sum_{j} c_{3-i,j}^{-2}}{\sum_{i,j} c_{i,j}^{-2}} \quad . \tag{8.34}$$

Rewriting equation 8.3 as

$$N_{1,j}(\omega,T)=\frac{\omega^2}{2\pi^2 v_{1,j}^3\left(\exp\left(\frac{\hbar\omega}{k_b T}\right)-1\right)} \tag{8.35}$$

and differentiating, results in

$$\frac{dN_{1,j}(\omega,T)}{dT}=\frac{\hbar\omega^3\exp\left(\frac{\hbar\omega}{k_b T}\right)}{2\pi^2 v_{1,j}^3 k T^2\left[\left(\exp\left(\frac{\hbar\omega}{k_b T}\right)-1\right)\right]^{-2}} \quad . \tag{8.36}$$

Next, 8.32 is numerically integrated evaluated using 8.36 and the reciprocal taken to get the value of the thermal boundary resistance.

8.4 Values of TBR from the literature and DMM

The diffuse mismatch model was chosen for this work, because it has shown some agreement with experimental values of TBR [25]. Table 8.1 gives typical values of TBR tabulated from the literature. The values obtained during the course of this work for TBR were between 1-2x$10^{-9}$$m^2$K/W. It can be seen that these values are in the same range as those found experimentally for material systems with similar mechanical properties. The value is, however, at least an order of magnitude smaller than the value of TBR found in mechanically dissimilar systems such as GaN/Si.

Interface	*TBR value (m^2K/W)*	*Method*	*Device*
This work	$1.2x10^{-9}$	DMM	EEL
GaAs/$Al_{0.33}Ga_{0.67}As$[25]	$0.48x10^{-9}$	Experiment	QCL
GaAs/$Al_{0.15}Ga_{0.85}As$[25]	$0.87x10^{-9}$	Experiment	QCL
InGaAs/AlInAs[25]	$4.4x10^{-9}$	Experiment	QCL
InGaAs/AlGaAsSb[25]	$0.93x10^{-9}$	Experiment	QCL
GaN/SiC[26]	$1.2x10^{-7}$	Experiment	HEMT
AlN/Si[26]	$7-8x10^{-8}$	Experiment	Thin film
GaN/Si[26]	$7x10^{-8}$	Experiment	HEMT

Table 8.1: Values of TBR available in the literature

8.5 Inclusion of thermal boundary resistance in device simulators

In order to accurately and efficiently include TBRs in our device simulator, a finite difference (FD) scheme has been adapted to model the thermal discontinuities introduced by the TBR at material interfaces. This scheme was originally proposed by Stern [27] to model the discontinuities in Quasi-TE modes of semiconductor waveguides. This approach accurately accounts for the step-wise gradient change in temperature at the material interfaces and the effect of TBR. At the boundaries between the calculation cells, temperature continuity is enforced, except at material interfaces, where there is a step proportional to the TBR.

Following Stern's work, it is assumed that each calculation cell "sees" [27] an apparent temperature T^* in the neighbouring cell. The * denotes that the temperature value is an apparent value and not the true value. (see figure 8.1) Thus, cell P "sees"

the temperature T^{*}_{r+1} in cell R and the temperature T_r in cell P. Conversely, cell R "sees" T^{*}_{r} in cell P and value T_{r+1} in cell R. These apparent temperatures, give a powerful way to include the boundary conditions at the cell interfaces within the discretisation scheme.

The general aim of the calculation is to obtain an expression for $T^{P}_{r+1/2}$ and $T^{R}_{r+1/2}$, and their derivatives on either side of the calculation cell interface, just inside cells P and R respectively. The temperatures and their derivatives are formulated in terms of real and apparent temperatures. The boundary condition due to the presence of TBR is applied at the interface

$$T^{(R)}_{r+1/2} - T^{(P)}_{r+1/2} = Rk_p \left(\frac{\partial T}{\partial x} \right)^{P}_{r+1/2} \quad . \tag{8.37}$$

The left hand side of equation 8.37 is the drop in temperature across the interface and the right hand side of the equation is the thermal boundary resistance multiplied by the heat flux. The resulting expression is then manipulated to give an effective temperature of T^{*}_{r+1}, which can be put straight into a finite difference scheme. The process is repeated at the interface of cell P and L.

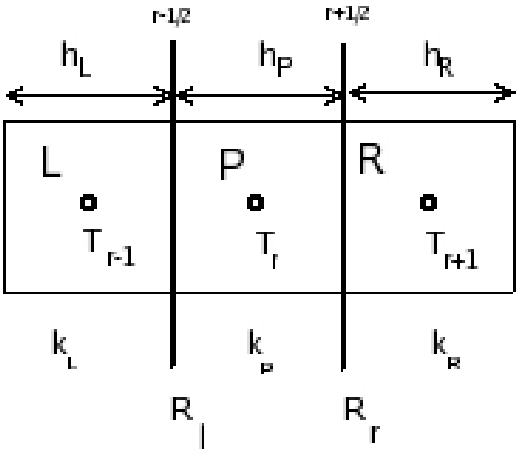

Figure 8.1: Diagram depicting 3 calculation cells.

Calculation of $T^{P}_{r+1/2}$:

The temperature that cell P "sees" in cell R can be described by the Taylor series expansion around the point *r+1/2* as

$$T^{*}_{r+1}=\sum_{r=0}^{\infty}\left(\frac{h_R}{2}\right)^{m}\left(\frac{\partial^{m}T}{\partial x^{m}}\right)^{(P)}_{r+1/2} \quad . \tag{8.38}$$

The first two terms in the series are,

$$T^{*}_{r+1}=T^{P}_{r+1/2}+\frac{h_R}{2}\left(\frac{\partial T}{\partial x^{m}}\right)^{(P)}_{r+1/2} \quad . \tag{8.39}$$

Therefore, rearranging to obtain $T^{P}_{r+1/2}$ gives

$$T^{P}_{r+1/2}=T^{*}_{r+1}-\frac{h_R}{2}\frac{\left(T^{*}_{r+1}-T_r\right)}{\frac{h_R+h_P}{2}} \tag{8.40}$$

or

$$T^{P}_{r+1/2}=T^{*}_{r+1}-\frac{h_R}{h_R+h_P}\left(T^{*}_{r+1}-T_r\right) \quad . \tag{8.41}$$

This can be rewritten as

$$T^{P}_{r+1/2} = T^{*}_{r+1}\left(1 - \frac{h_R}{h_P + h_R}\right) + T_r \frac{h_R}{h_P + h_R} \quad . \tag{8.42}$$

Calculation of $T^{R}_{r+1/2}$:

The temperature that cell R "sees" in cell R can be described by the Taylor series expansion around the point r+1/2 as

$$T_{r+1} = \sum_{m=0}^{\infty} \left(\frac{h_R}{2}\right)^m \left(\frac{\partial^m T}{\partial x^m}\right)^{(R)}_{r+1/2} \tag{8.43}$$

$$T_{r+1} = T^{R}_{r+1/2} + \left(\frac{h_R}{h_P + h_R}\right)\left(T_{(r+1)} - T^{*}_{r}\right) \tag{8.44}$$

$$T^{R}_{r+1/2} = T_{r+1}\left(1 - \frac{h_R}{h_P + h_R}\right) + T^{*}_{r}\frac{h_R}{h_R + h_P} \tag{8.45}$$

Calculation of $(\partial T/\partial x)^{(R)}_{r+1/2}$:

Using a similar method as used to obtain $T^{P}_{r+1/2}$ and $T^{R}_{r+1/2}$, the expressions for the derivatives of temperature on either side of the interface are obtained. The temperature cell R sees in cell P can be written in a Taylor expansion as

$$T^{*}_{r} = \sum_{m=0}^{\infty} \left(\frac{-h_p}{2}\right)^m \left(\frac{\partial^m T}{\partial x^m}\right)^{(R)}_{r+1/2} \quad . \tag{8.46}$$

The first two terms of the series are

$$T^{*}_{r} = T^{(R)}_{r+\frac{1}{2}} - \frac{h_p}{2}\left(\frac{\partial T}{\partial x^m}\right)^{(R)}_{r+1/2} \tag{8.47}$$

and using 8.44

$$T_r^* = T_{r+1}\left(1 - \frac{h_R}{h_P + h_R}\right) + T_r^* \frac{h_R}{h_P + h_R} - \frac{h_P}{2}\left(\frac{\partial T}{\partial x}\right)_{r+1/2}^{(R)} \tag{8.48}$$

$$\frac{h_p}{2}\left(\frac{\partial T}{\partial x}\right)_{r+1/2}^{(R)} = T_{t+1}\left(1 - \frac{h_R}{h_P + h_R}\right) + T_r^*\left(\frac{h_R}{h_P + h_R} - 1\right) \quad , \tag{8.49}$$

which can be rewritten as

$$\left(\frac{\partial T}{\partial x}\right)_{r+1/2}^{(R)} = \left(T_{t+1} - T_r^*\right)\left(1 - \frac{h_R}{h_P + h_R}\right)\frac{2}{h_p} \quad . \tag{8.50}$$

Calculation of $(\partial T/\partial x)^{(P)}_{r+1/2}$:

The temperature cell P 'sees' from cell P is given by

$$T_r = \sum_{m=0}^{\infty}\left(\frac{-h_p}{2}\right)^m \left(\frac{\partial^m T}{\partial x^m}\right)_{r+1/2}^{(R)} \tag{8.51}$$

$$T_r = T_{r+\frac{1}{2}}^{(P)} - \frac{h_P}{2}\left(\frac{\partial T}{\partial x}\right)_{r+1/2}^{(P)} \tag{8.52}$$

then using 8.42

$$T_r = T_{r+1}^*\left(1 - \frac{h_R}{h_P + h_R}\right) + T_r \frac{h_R}{h_P + h_R} - \frac{h_P}{2}\left(\frac{\partial T}{\partial x}\right)_{r+1/2}^{(P)} \tag{8.53}$$

and rearranging we obtain

$$\left(\frac{\partial T_x}{\partial x}\right)_{r+1/2}^{P} = \frac{2}{h_P}\left(1 - \frac{h_R}{h_P + h_R}\right)\left(T_{r+1}^* - T_r\right) \quad . \tag{8.54}$$

Applying the boundary conditions around cell r+1/2

Four expressions linking, temperatures $T^P_{r+1/2}$ and $T^R_{r+1/2}$ and their derivatives have now been obtained. Two boundary conditions are now applied. The 1st boundary

condition enforces the continuity of temperature except at material interfaces where it is proportional to the heat flux.

$$T_{r+1/2}^{(R)} - T_{r+1/2}^{(P)} = Rk_p \left(\frac{\partial T}{\partial x} \right)_{r+1/2}^{P} \quad . \tag{8.55}$$

The 2nd boundary condition enforces the continuity of net heat flux across material interfaces

$$\left(\frac{\partial T}{\partial x} \right)_{r+1/2}^{P} k_P = k_R \left(\frac{\partial T}{\partial x} \right)_{r+1/2}^{R} \quad . \tag{8.56}$$

Therefore, from 8.56, 8.54 and 8.42

$$T_r^* = T_{r+1} - \frac{k_P}{k_R} (T_{r+1}^* - T_r) \quad . \tag{8.57}$$

Then, rewriting 8.55 with 8.50, 8.54

$$\begin{aligned} T_{r+1}\left(1 - \frac{h_R}{h_P + h_R}\right) + T_r^* \frac{h_R}{h_P + h_R} - T_{r+1}^*\left(1 - \frac{h_R}{h_P + h_R}\right) - T_r\left(\frac{h_R}{h_P + h_R}\right) = \\ \frac{Rk_P 2}{h_P}\left(1 - \frac{h_R}{h_P + h_R}\right)(T_{r+1}^* - T_r) \end{aligned} \quad . \tag{8.58}$$

After rearranging and using 8.57, one obtains

$$T_{r+1}^* = \frac{T_{r+1} - T_r\left(\frac{h_R}{h_P + h_R}\left(1 - \frac{k_P}{k_R}\right) - \frac{2Rk_P}{h_P}\left(1 - \frac{h_R}{h_P + h_R}\right)\right)}{\frac{h_R}{h_P + h_R}\left(\frac{k_P}{k_R} - 1\right) + 1 + \frac{2\mathrm{Rk}_P}{h_P}\left(1 - \frac{h_R}{h_P + h_R}\right)} \quad , \tag{8.59}$$

which is the temperature cell P 'sees' in terms of T_{r+1} and T_r after taking into account the thermal boundary resistance. Exactly the same process is followed again to obtain a value of T_{r-1}^* in terms of T_{r-1} and T_r for the interface between cells L and P.

Calculation of $T^{P}_{r-1/2}$:

$$T_r = \sum_{m=0}^{\infty} \left(\frac{h_P}{2}\right)^m \left(\frac{\partial^m T}{\partial x^m}\right)^{(P)}_{r-1/2} \tag{8.60}$$

$$T_r = T^{P}_{r-1/2} + \frac{h_p}{2}\left(\frac{\partial T}{\partial x}\right)^{(P)}_{r-1/2} \tag{8.61}$$

$$T_r = T^{P}_{r-1/2} + \frac{h_P}{h_L + h_P}\left(T_r - T^{*}_{r-1}\right) \tag{8.62}$$

$$T^{P}_{r-1/2} = T_r - \frac{h_P}{h_L + h_P}\left(T_r - T^{*}_{r-1}\right) \tag{8.63}$$

$$T^{P}_{r-1/2} = T_r\left(1 - \frac{h_P}{h_L + h_P}\right) + \frac{h_P}{h_L + h_P} T^{*}_{r-1} \tag{8.64}$$

Calculation of $(\partial T/\partial x)^{(P)}_{r-1/2}$:

$$T^{*}_{r-1} = \sum_{m=0}^{\infty} \left(-\frac{h_L}{2}\right)^m \left(\frac{\partial^m T}{\partial x^m}\right)^{\mathrm{P}}_{\mathrm{r\text{-}1/2}} \tag{8.65}$$

$$T^{*}_{r-1} = T^{\mathrm{P}}_{r-1/2} - \frac{h_L}{2}\left(\frac{\partial T}{\partial x}\right)^{P}_{r-1/2} \tag{8.66}$$

$$\frac{h_L}{2}\left(\frac{\partial T}{\partial x}\right)^{P}_{r-1/2} = T^{P}_{r-1/2} - T^{*}_{r-1} \tag{8.67}$$

Using 8.64 we obtain,

$$\frac{h_L}{2}\left(\frac{\partial T}{\partial x}\right)^{P}_{r-1/2} = T_r\left(1 - \frac{h_P}{h_L + h_P}\right) - T^{*}_{r-1}\left(1 - \frac{h_P}{h_L + h_P}\right) \tag{8.68}$$

$$\left(\frac{\partial T}{\partial x}\right)^{P}_{r-1/2} = \frac{2}{h_L}\left(1 - \frac{h_P}{h_L + h_P}\right)\left(T_r - T^{*}_{r-1}\right) \tag{8.69}$$

Calculation of $T^{l}_{r-1/2}$:

$$T_r^* = \sum_{m=0}^{\infty} \left(\frac{h_P}{2} \right)^m \left(\frac{\partial^m T}{\partial x^m} \right)_{r-1/2}^{(L)} \tag{8.70}$$

$$T_r^* = T_{r-1/2}^{(L)} + \frac{h_p}{h_P + h_L} \left(T_r^* - T_{r-1} \right) \tag{8.71}$$

$$T_{r-1/2}^{L} = T_r^* \left(1 - \frac{h_P}{h_P + h_L} \right) + \frac{h_P}{h_P + h_L} T_{r-1} \tag{8.72}$$

Calculation of $(\partial T/\partial x)^{(L)}_{r-1/2}$:

$$T_{r-1} = \sum_{m=0}^{\infty} \left(\frac{-h_L}{2} \right)^m \left(\frac{\partial^m T}{\partial x^m} \right)_{r-1/2}^{L} \tag{8.73}$$

$$T_{r-1} = T_{r-1/2}^{L} - \frac{h_L}{2} \left(\frac{\partial T}{\partial x} \right)_{r-1/2}^{L} \tag{8.74}$$

Using equation 8.72, we obtain

$$\frac{h_L}{2} \left(\frac{\partial T}{\partial x} \right)_{r-1/2}^{L} = T_{r-1/2}^{L} - T_{r-1} \tag{8.75}$$

$$\frac{h_L}{2} \left(\frac{\partial T}{\partial x} \right)_{r-1/2}^{L} = T_r^* \left(1 - \frac{h_P}{h_P + h_L} \right) + \frac{h_P}{h_P + h_L} T_{r-1} - T_{r-1} \tag{8.76}$$

$$\left(\frac{\partial T}{\partial x} \right)_{r-1/2}^{L} = \frac{2}{h_L} \left(1 - \frac{h_P}{h_P + h_L} \right) \left(T_{r-1} - T_{r-1} \right) \tag{8.77}$$

The boundary conditions are applied at point r-1/2

As above, the boundary conditions of continuity of temperature, except at a TBR and continuity of heat flux are applied.

1st boundary condition

$$T^{\mathrm{P}}_{x-1/2} - T^{L}_{x-1/2} = R_L k_L \left(\frac{\partial T}{\partial x} \right)^{(L)}_{r-1/2} \tag{8.78}$$

2nd boundary condition

$$\left(\frac{\partial T}{\partial x} \right)^{L}_{r-1/2} k_L = k_P \left(\frac{\partial T}{\partial x} \right)^{P}_{r-1/2} \tag{8.79}$$

Using 8.79, 8.77 and 8.69, one obtains,

$$T^*_r = \frac{k_P}{k_L} \left(T_r - T^*_{r-1} \right) + T_{r-1} \tag{8.80}$$

$$\begin{aligned} & T_r \left(1 - \frac{h_P}{h_P + h_L} \right) + T^*_{r-1} \frac{h_P}{h_L + h_P} - T^*_r \left(1 - \frac{h_P}{h_P + h_L} \right) - \frac{h_P}{h_P + h_L} T_{r-1} \\ & = \frac{2 R_L k_L}{h_L} \left(1 - \frac{h_P}{h_P + h_L} \right) \left(T^*_r - T_{r-1} \right) \end{aligned} \tag{8.81}$$

Then using 8.80 and rearranging one obtains,

$$T^*_{r-1} = \frac{T_{r-1} - T_r \left(1 - \frac{h_P}{h_L + h_P} - \frac{k_P}{k_L} \left(1 - \frac{h_P}{h_P + h_L} \right) - \frac{2 R_L k_p}{h_L} \left(1 - \frac{h_P}{h_P + h_L} \right) \right)}{\frac{h_P}{h_L + h_P} + \frac{k_P}{k_L} \left(1 - \frac{h_P}{h_P + h_L} \right) + \frac{2 R_L k_P}{h_L} \left(1 - \frac{h_P}{h_P + h_L} \right)} \tag{8.82}$$

using

$$1 - \frac{h_P}{h_L + h_P} = \frac{h_L}{h_L + h_P} \tag{8.83}$$

$$\text{and} \quad 1 - \frac{h_L}{h_L + h_P} = \frac{h_P}{h_L + h_P} \quad . \tag{8.84}$$

Finally, equation 8.82 may be rewritten as,

$$T^*_{r-1}=\frac{T_{r-1}-T_r\left(\frac{h_L}{h_L+h_P}\left(1-\frac{k_P}{k_L}\right)-\frac{2R_Lk_p}{h_L}\left(1-\frac{h_P}{h_P+h_L}\right)\right)}{\frac{h_L}{h_L+h_P}\left(\frac{k_P}{k_L}-1\right)+1+\frac{2R_Lk_P}{h_L}\left(1-\frac{h_P}{h_P+h_L}\right)} \quad . \qquad (8.85)$$

The temperatures that a cell P "sees" either side of it have been described. The expressions for T^*_{r-1} and T^*_{r+1} can be substituted into the usual finite difference scheme

$$\frac{\partial}{\partial x}k_r\frac{\partial}{\partial x}T_r=2k_r\frac{\Delta x_1T^*_{r+1}-T_r(\Delta x_2+\Delta x_1)+\Delta x_2T^*_{r-1}}{(\Delta x_1+\Delta x_2)\Delta x_1\Delta x_2}+O(h_x^2) \quad , (8.86)$$

where Δx_1 and Δx_2 have been redefined as

$$\Delta x_1=\frac{h_L}{2}+\frac{h_P}{2} \qquad (8.87)$$

$$\text{and} \quad \Delta x_2=\frac{h_P}{2}+\frac{h_R}{2} \quad . \qquad (8.88)$$

The above derivation was only performed for the 1D case. However, using the superposition principle, this derivation can be extended to the 2D or even the 3D case. The result of the above derivation is a numerically simple and robust discretisation scheme, taking into account TBR at the material interfaces.

8.6 Validation of numerical scheme

In this section, analytical and numerical solutions of a thermal problem including a TBR are compared to demonstrate the accuracy of the discretisation scheme. The 1D heat conduction equation is given as

$$Q=-kA\frac{dT}{dx} \quad , \qquad (8.89)$$

where Q is the total heat flowing through cross-section A. By solving 8.89 and 8.1 with appropriate boundary conditions, analytical solutions for simple thermal problems can be obtained. For the purpose of this comparison, a material system comprised of a 100µm thick slab of GaN joined to a 100µm thick slab of SiC was modelled. The cross-sectional area of the slabs considered was 1mmx100µm. The thermal conductivities are given in table 8.2 and the TBR at the GaN/SiC interface was taken as $1.2 \times 10^{-9} Km^2/W$.

Material	Thermal Conductivity W/m/k
SiC	350 [28]
GaN	130 [28]

Table 8.2: Simulation parameters.

A uniform heat flow of 1W was simulated flowing through the two slabs. This heat flowed from a source in perfect contact with the GaN to a perfect heat sink in contact with the exposed surface of the SiC. The exposed surface of the SiC was held at 300K. The calculation was performed at a high temperature (>300K) to highlight the applicability of the method to device simulation. Nevertheless, this scheme is equally applicable to low temperature systems.

A comparison of the numerically calculated and analytical solutions are shown in figure 8.2. It shows good agreement between the analytical and numerical results. Note that the presence of the TBR results in a sudden drop in temperature across the boundary and also that there is a change in the gradient of the temperature exactly at the interface between the two materials.

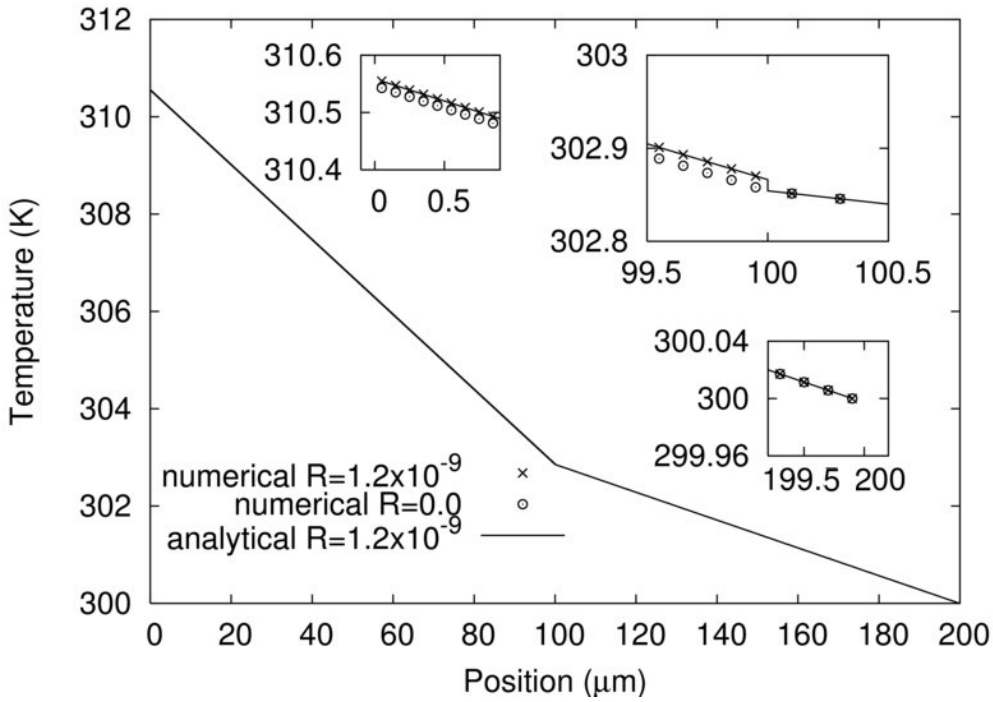

Figure 8.2: Comparison of numerical and analytical solution of heat flux

Also included in figure 8.2 for comparison, is a numerical result that was calculated without including TBR. It can be seen that an error of the order of 10mK is introduced into the simulation by not including TBR at the interface.

8.7 The impact of TBR on a device with multiple epitaxial layers

In this section, a more complex example is demonstrated. A structure is simulated that contains multiple epitaxial layers, such as would be found in a VCSEL mirror. In this example, only the thermal problem is solved (i.e. not the electrical problem). Figure 8.3 plots the thermal profile across a structure with 30 epitaxial layers of GaAs/AlAs. In one simulation, the impact of TBR has been included and in the other the impact of TBR has not been included. Figure 8.4 shows a zoomed in section of the graph where the impact of TBR can be seen. This shows a 5K increase in temperature

across the structure due to the inclusion of TBR. The value of TBR was calculated from the DMM model for each epitaxial interface.

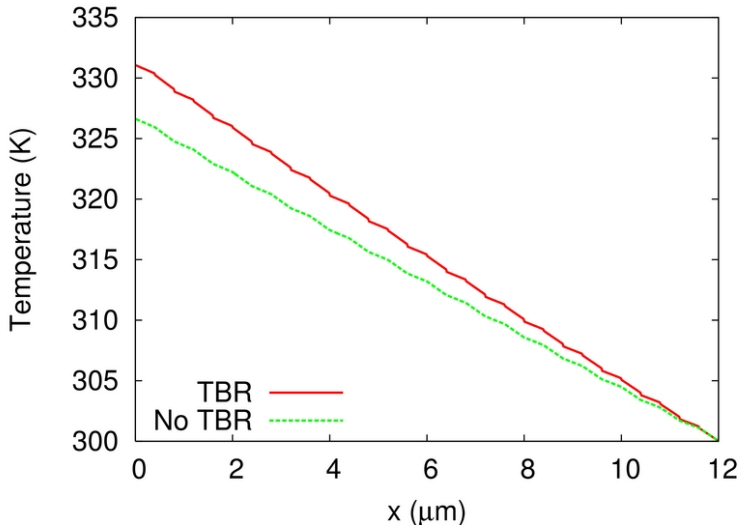

Figure 8.3: The thermal profile across a structure with and without TBR included.

The inclusion of TBR has a two-fold impact on the simulation. Firstly, there is a temperature rise due to the phonon reflections at the interface. There is also a secondary effect because the device is hotter due to the TBR. The lattice conductivity decreases with temperature, thereby pushing up the device temperature further. This can be seen in figure 8.5, where the thermal conductivity of the bulk layers has been plotted.

The predicted thermal conductivity for structures of the same width, but with increasing number of DBR mirror layers (thus interfaces) is plotted in figure 8.6. It

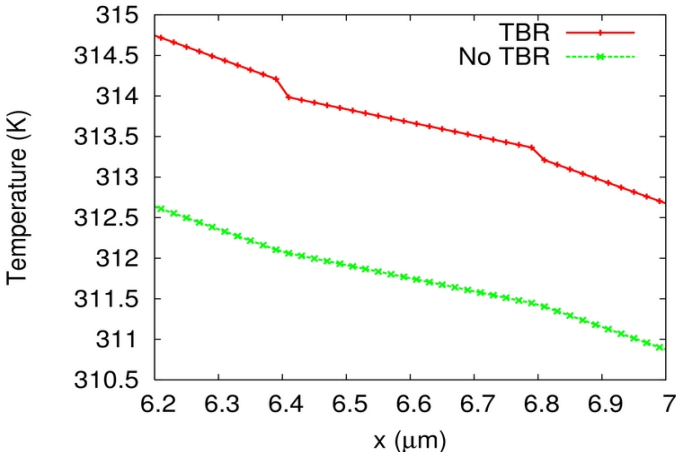

Figure 8.4: A zoomed in section of figure 8.3, the temperature steps caused by TBR can clearly be seen in the figure.

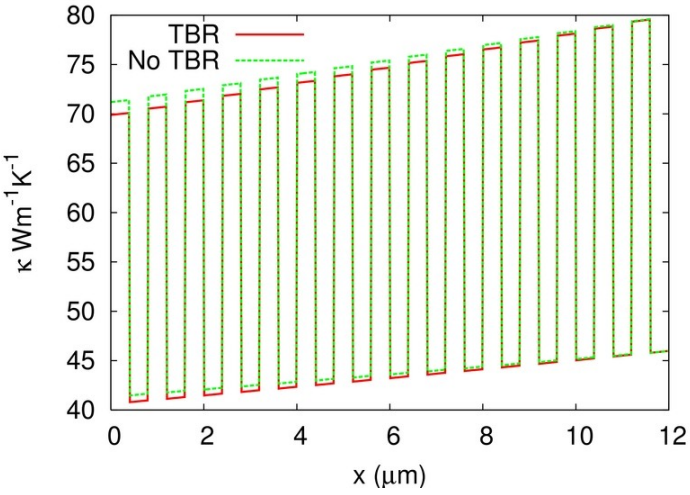

Figure 8.5: The predicted thermal conductivity of a 30 layer VCSEL.

can be seen that even for 30 interfaces, the thermal conductivity has been reduced by 15%.

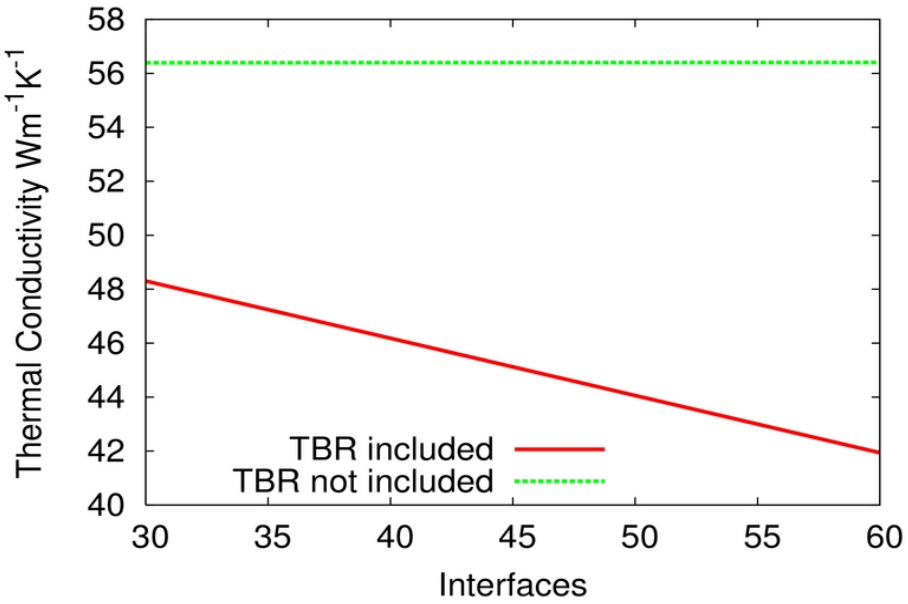

Figure 8.6: Average thermal conductivity across the DBR mirror as the number of layers is increased and the thickness of the structure kept the same (red line). Plotted on the same graph is a line indicating the predicted thermal conductivity of the structure when TBR is not included. (green line).

8.8 Inclusion of the impact of TBR within a full device simulator

In this section, the discretisation scheme developed in Section 8.5 is included in our 2D (lateral and vertical) laser diode simulation tool developed in chapter 5-7. It self-consistently solves the carrier continuity, drift-diffusion, Poisson's, lattice heat flux, quantum well capture/escape and photon rate equations. The heat sources and the continuity equations have been derived from a moment expansion of the Boltzmann transport equation. The valance band structure of the QW is calculated using a 4x4 band ***k.p*** model, while the conduction band structure is calculated using a band anti-crossing model. Gain and spontaneous emission are calculated from the band structure using Fermi-Dirac statistics and Fermi's golden rule.

The specific devices investigated were 1.3μm dilute nitride edge-emitting double

quantum well lasers with 7nm $Ga_{0.613}In_{0.387}N_{0.012}As$ quantum wells. The GaAs confinement regions were 20nm thick and were surrounded by 160nm thick compositionally graded AlGaAs layers. Figure 8.7 shows the epitaxial structure of the device. The ridge width measured 3.2µm and was etched to a depth of 1.3µm. The etched trenches were filled with a polymer with a low thermal conductivity, which was assumed to be $1x10^{-6}$ W/(mK). The uncoated facets were assumed to have a reflectivity of R=0.32. These devices are operated with a typical front facet output power of P_{out}=10–15mW.

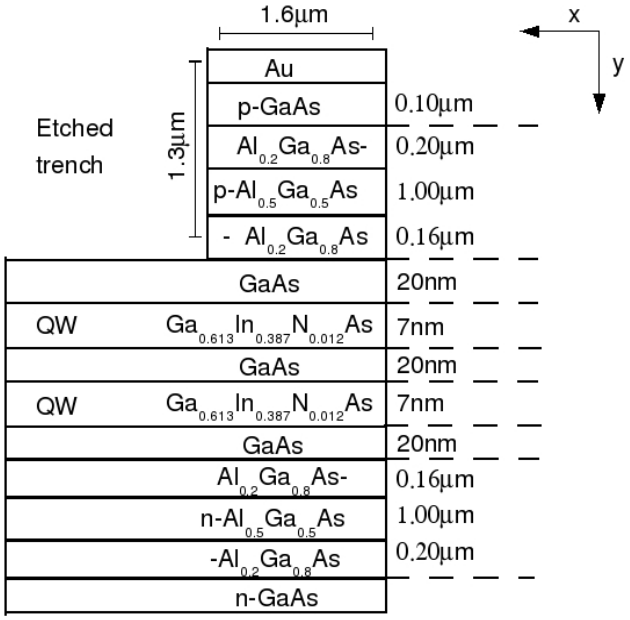

Figure 8.7: Device structure. The dashed lines indicate where TBRs were introduced. The device is symmetrical about the y-axis and only the left half is shown in this figure.

For the simulations, a heat sink with a thermal resistance of 1K/W coupled to a 300K reservoir was used to approximate the heat leaving the device. A typical simulated L-I

curve is shown in figure 8.8. The isothermal simulation refers to a simulation where the lattice thermal profile across the device is set at 300K (experimentally such a curve could be obtained by running the laser with a pulsed current with a very low duty cycle). The curve labelled thermal simulation refers to the case where the lattice heat equation has been solved throughout the device and corresponds to the laser operating in CW. The observed roll over is predominantly due to the thermal dependence of the gain and the increase of the Auger and Shockley-Read-Hall recombination rates with temperature.

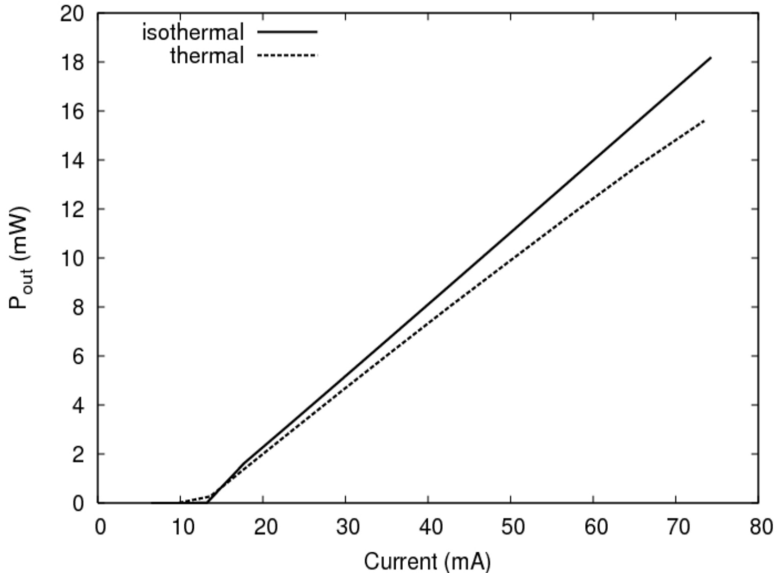

Figure 8.8: Typical isothermal and thermal L-I curves.

A simulated 2D thermal profile of a device is shown in figure 8.Error: Reference source not found without correcting for TBR. The device is producing 14mW of optical power at the front facet from an injection current of 65mA. As the simulation is performed in half-space, only half the ridge and one etched trench are visible in the

plot. The simulation area corresponds to the structure shown in figure 8.7. The polymer filled etch trench is indicated with a dotted box. The QWs are just below the etch trench within the dense mesh. The area of high temperature to the right of the etch trench is the ridge waveguide.

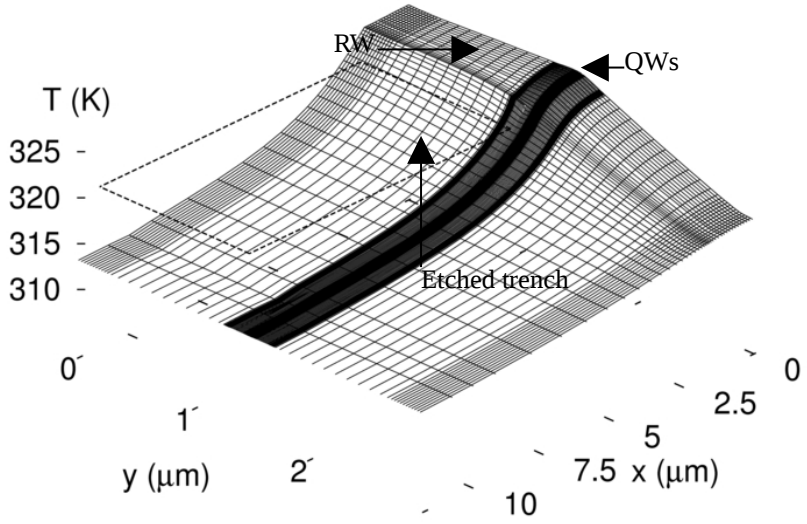

Figure 8.7: Half-space 2D thermal profile without including the effect of TBR. The simulation window corresponds to the area shown in Figure 1. The area in the box represents the filled etched trench.

The simulation was repeated, but correcting for the impact of TBR. Figure 8.9 shows a vertical temperature profile through the centre of the device (x=0) for the 2D simulations with and without TBR. The inclusion of TBR results in a higher predicted QW/ridge temperature. The abrupt temperature steps at the QW/confinement interfaces due to TBR are visible in the magnified section of the figure.

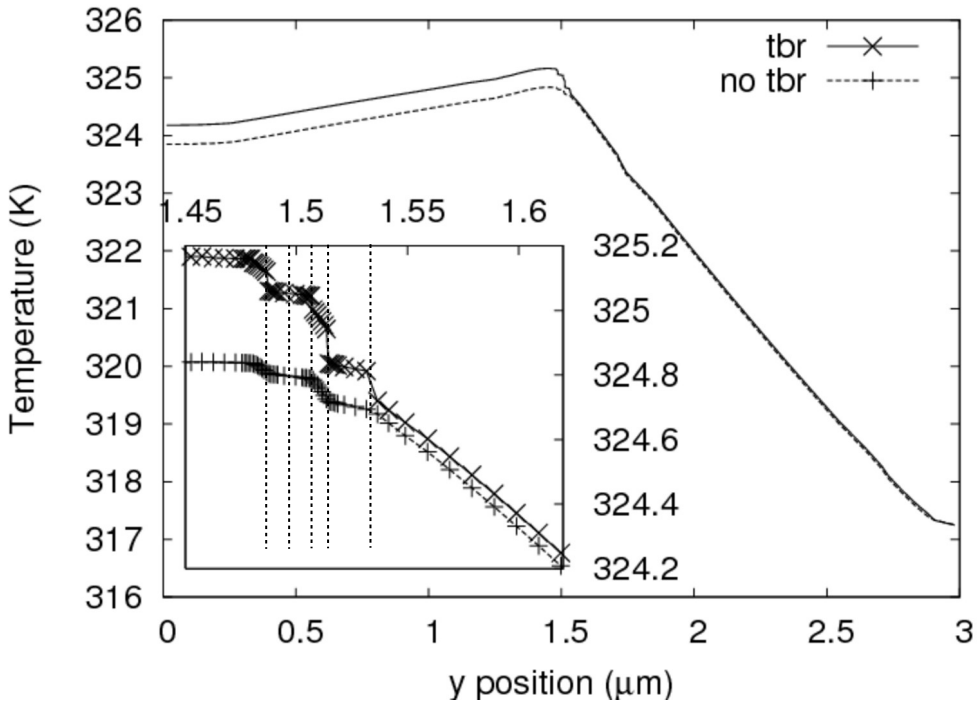

Figure 8.9: A slice through the 2D simulation profile taken in the centre of the device. Simulations with and without TBR are shown. Epilayer interfaces are indicated with dotted vertical lines. Abrupt temperature steps are visible at the QW/confinement layer interfaces. The values of TBR were calculated using DMM theory as a function of interface temperature.

The relative increase in the 2D temperature profile due to the inclusion of TBR is plotted in figure 8.Error: Reference source not found. The rapid rise in temperature under the ridge is due to a combination of the multiple material interfaces surrounding the QWs at the bottom of the ridge and the high heat flux due to high rates of Joule heating and free carrier absorption within the ridge. The increase in the predicted QW temperature due to the inclusion of TBR is plotted as a function of injection current in figure 8.Error: Reference source not found. As discussed earlier, the exact TBR of the interfaces are not known due to the lack of experimental data. Therefore, a range of TBR values were simulated. TBR values 1, 2, 4 and 8 times larger that that predicted by the DMM were used.

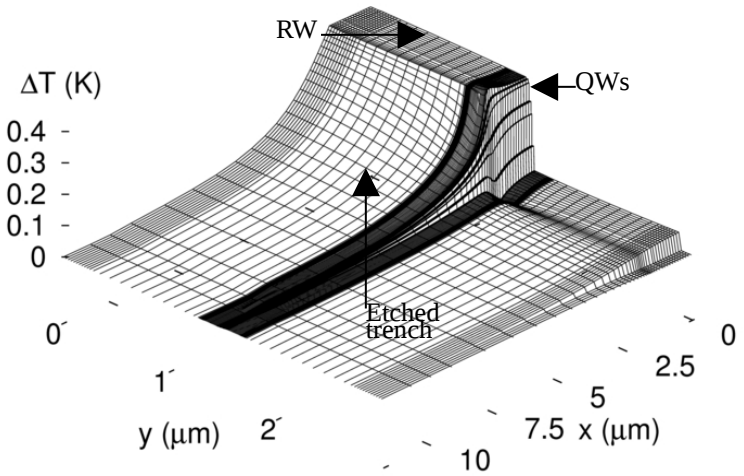

Figure 8.10: Difference in 2D thermal profiles due to the inclusion of TBR as predicted by the DMM.

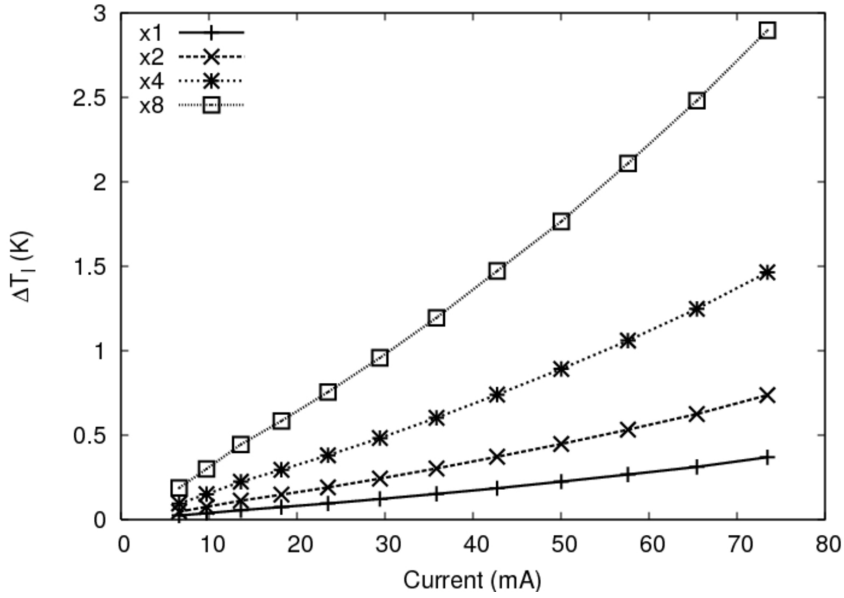

Figure 8.11: Difference in average quantum well temperature between simulations including TBR and not including TBR as a function of current. The curve labeled x1 is that predicted using DMM theory and x8 is that predicted using a value of TBR x8 bigger than that predicted by DMM.

Figure 8.12 shows the corresponding change in the light-current (L-I) curves with and without TBR. TBR causes a larger reduction in the light output at higher currents because the heat flux flowing down the ridge and across the epitaxial interfaces of the QWs is larger. Thus, the temperature drop across the TBRs is also larger.

In order to investigate the impact of more epitaxial interfaces on the predicted temperature, a device with four quantum wells was simulated. The difference in QW temperature due to the inclusion of TBR for devices with 2 and 4 quantum wells is plotted in Figure 8.13. With an increasing number of quantum wells, and thus interfaces, the discrepancy in temperature is increased from ~0.3K to ~0.4K.

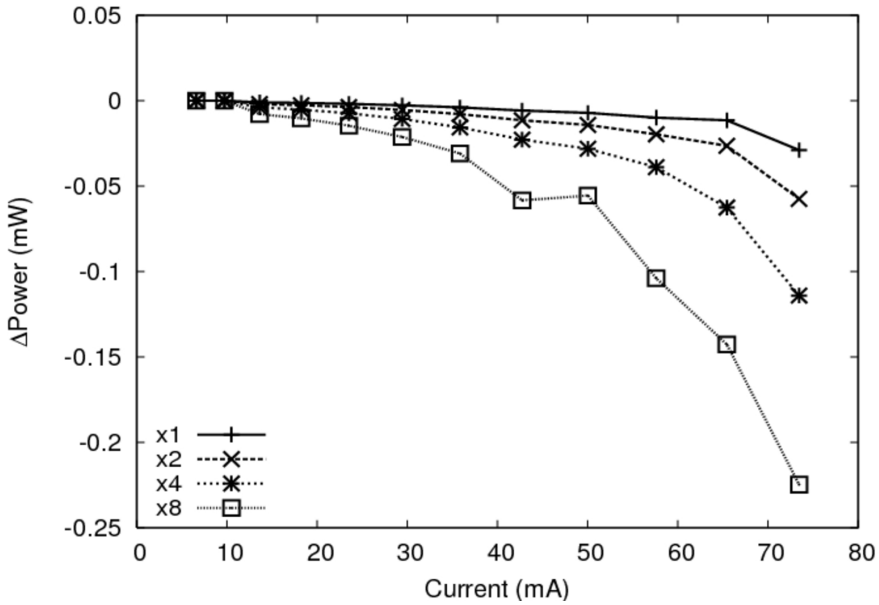

Figure 8.12: Change in L-I curves due to the inclusion of TBR. The curve labeled x1 is that predicted using DMM theory and x8 is that predicted using a value of TBR x8 bigger that predicted by DMM.

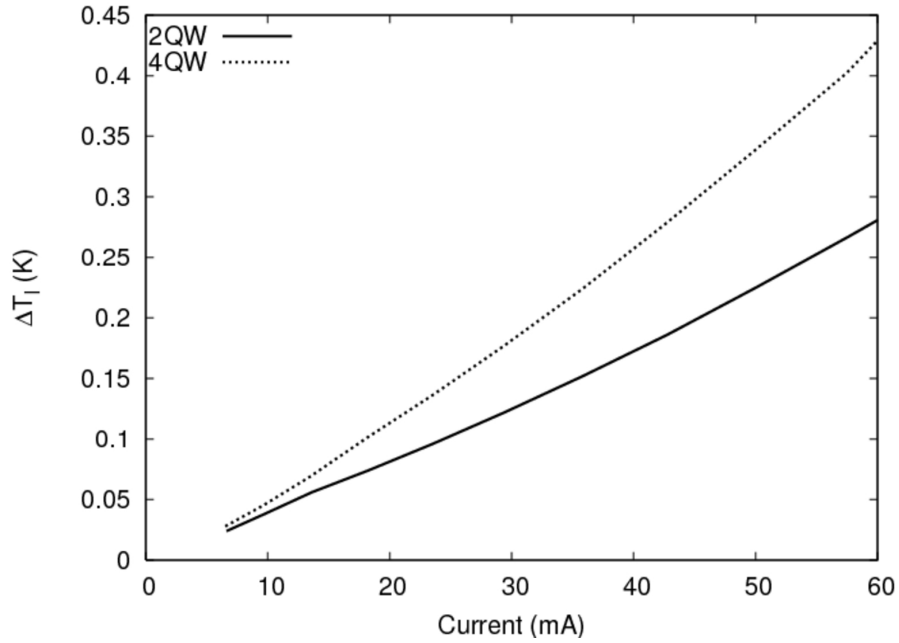

Figure 8.13: Difference in the QW temperature between simulations that include and neglect TBR for devices with 2 and 4 QWs. The values of TBR were predicted using DMM.

8.9 The impact of TBR on high power high brightness 980nm ridge waveguide lasers

The 1.3μm device investigated in the previous section is a low power device. The device is typically not to be driven hard, therefore little heat is generated. Thus, it would be expected that the amount of heat flux would be low and as such the impact of TBR would be low. In this section, the impact of TBR on a high power 980nm ridge waveguide device is considered. High-power, single mode 980nm laser diodes are primarily used for pumping erbium doped fibre amplifiers (EDFAs) in telecommunication networks. Modern commercial 980nm pump lasers can deliver up to 1.2W of output power with lifetimes in excess of 10,000 hours, while output powers of up to 1.8W have been reported [29]. In order to achieve the long lifetimes required by the telecommunications industry, laser structures must be optically,

electrically and thermally optimised. The use of accurate and predictive device simulation tools is invaluable during the optimisation and design stages.

The device studied in this work is based on an epitaxy presented elsewhere [30]. In brief, it consists of a single 9nm InGaAs QW with 0.16μm thick InGaAsP confinement regions and 1.5μm thick InGaP cladding regions-all grown on a GaAs substrate. The RW device studied here has a 2mm long stripe, which is 3μm wide. The back and front facet reflectivities are 0.90 and 0.03, respectively. A total of seven interfaces are present within the laser structure. At each of these epitaxial interfaces, a TBR was introduced. In this work, we use the Diffuse Mismatch Model [10] to estimate the values of TBR associated with each interface. Although the values of TBR predicted by DMM vary as a function of material composition and temperature DMM predicts values of around ~$1x10^{-9} m^2K/W$ for the interfaces within the structure. For the purpose of the simulations here, it is assumed that the devices are mounted p-side down on a heatsink stabilised at a temperature of 300K.

A series of simulations were again performed at different biases with and without including TBR. A simulated L-I curve where thermal boundary resistance has been neglected is plotted in figure 8.14. A gradual roll-over in the output power is observed and an output power of >1W is achieved. The simulations were repeated including TBR and in figure 8.15 the impact of this on the L-I curve is shown. At low injection currents, where there is little device heating and thus low heat flux, the impact of TBR on the L-I curve is small. However, as heat generation increases, the impact of TBR

manifests itself as a reduction in the optical output power of up to 0.6mW. In figure 8.16, the lattice temperature T_l, LO-phonon temperature T_{LO}, electron temperature T_e and hole temperature T_h are plotted as a function of injection current for a point located in the QW at the centre of the device. In this simulation the effects of TBR are neglected. It can be seen that the electron and hole temperatures 'ride' on the hot LO-phonon temperature [32].

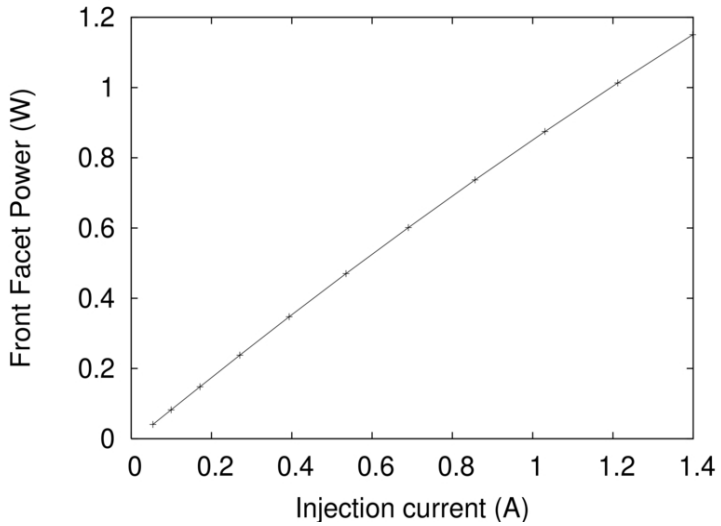

Figure 8.14: L-I curve for a device simulation where TBR is neglected.

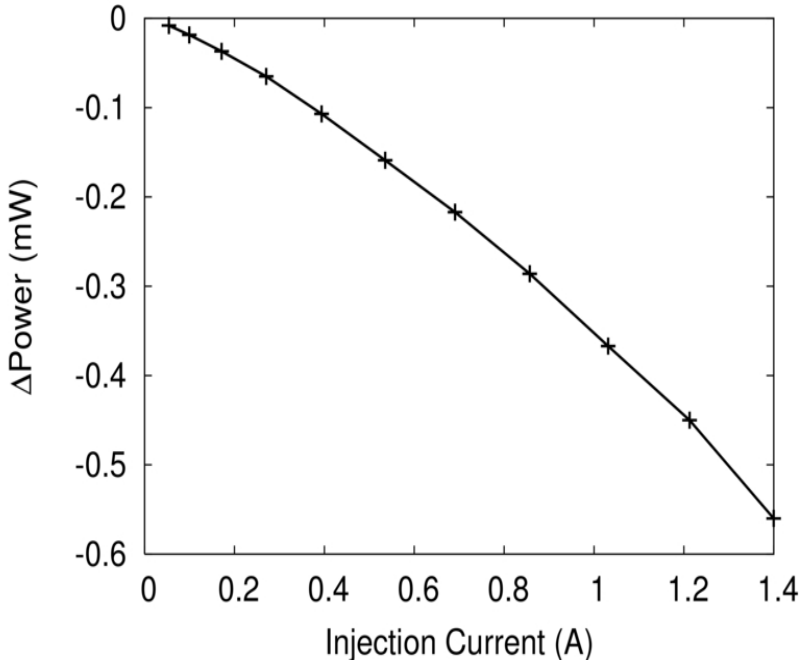

Figure 8.15: Change in the optical power due to the impact of TBR.

As the injection current increases, so does the impact of the hot phonon bottleneck. Figure 8.17 then plots the difference in the four temperatures as a function of injection current for the case when TBR has been included in the simulation. In this case, it can be seen that the lattice temperature is affected the most by TBR.

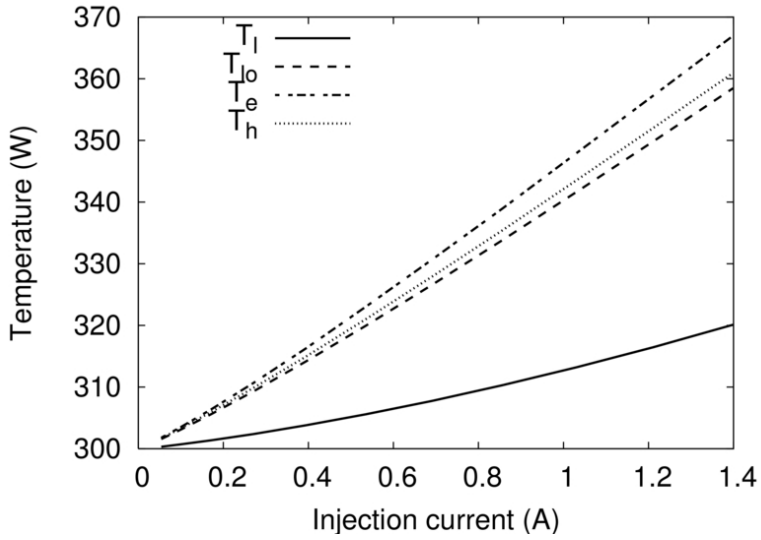

Figure 8.16: QW temperatures (T_l, T_e, T_h, T_{LO}) plotted as a function of injection current for the case where TBR has been neglected.

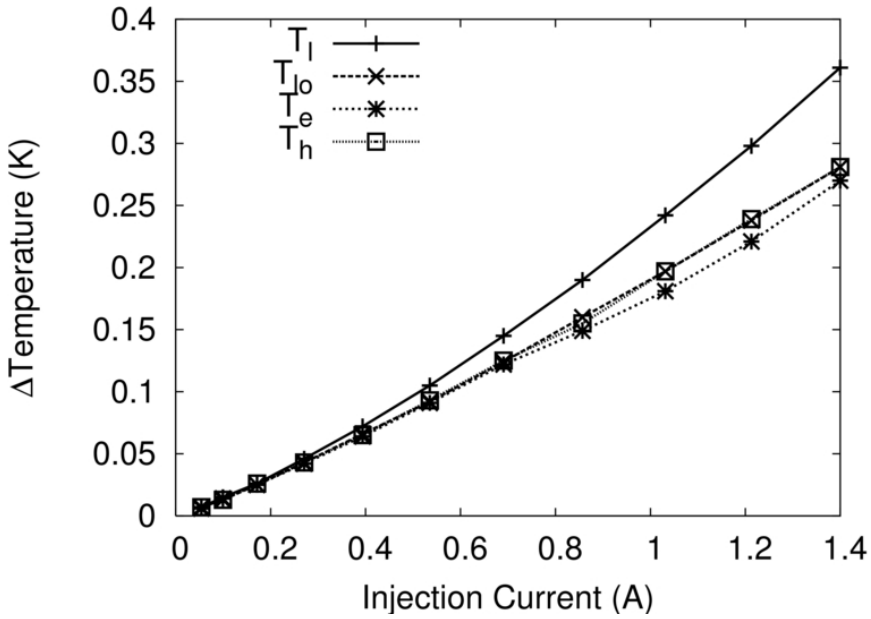

Figure 8.17: Increases in temperatures due to TBR.

Figure 8.18 plots the thermal profile down through the epitaxial layer sequence for simulations with and without TBR. Figure 8.19 shows a zoomed in section of the QW region, where a sudden jump in the lattice temperature caused by the introduction of TBR can be seen.

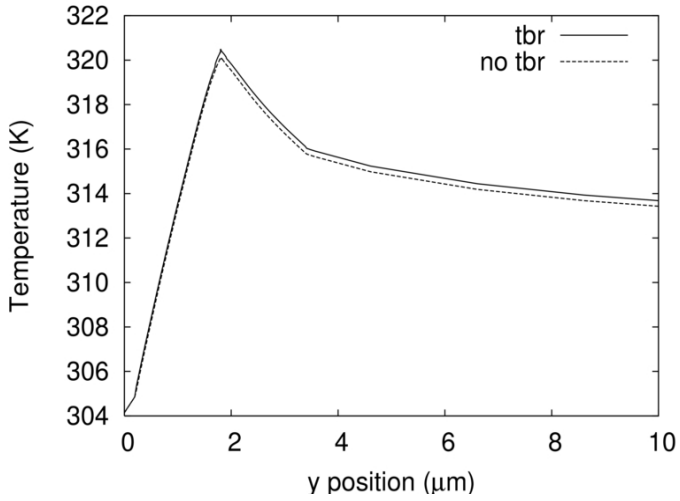

Figure 8.18: Thermal profile through the epitaxial layer sequence for simulations with and without TBR. These profiles were obtained for an injection current of 1.4A.

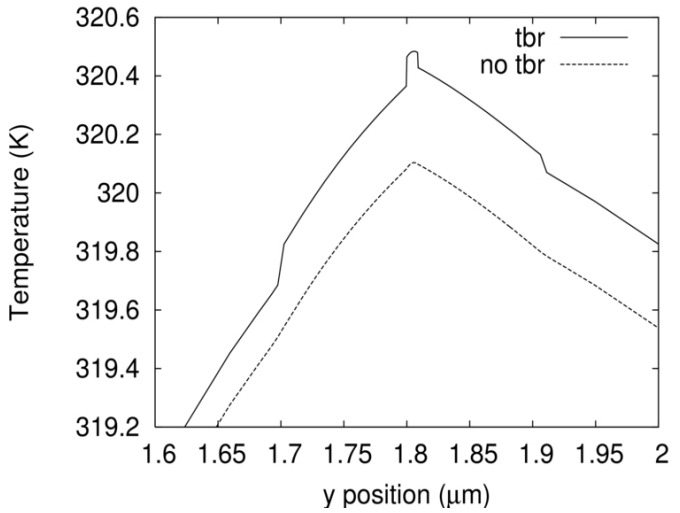

Figure 8.19: Zoomed in section of the QW region. These profiles were obtained for an injection current of 1.4A

Figure 8.20 plots the QW temperatures laterally across half of the device (where 0μm corresponds to the centre of the RW) as obtained from the simulations where TBR was neglected. Figure 8.21 then shows the difference in the lateral QW temperature profiles caused by the inclusion of TBR. The impact of the large LO-phonon bottleneck can be seen elevating the electron and hole temperatures in the centre of the device where carrier capture is at its greatest and hence LO-phonon generation is at a maximum.

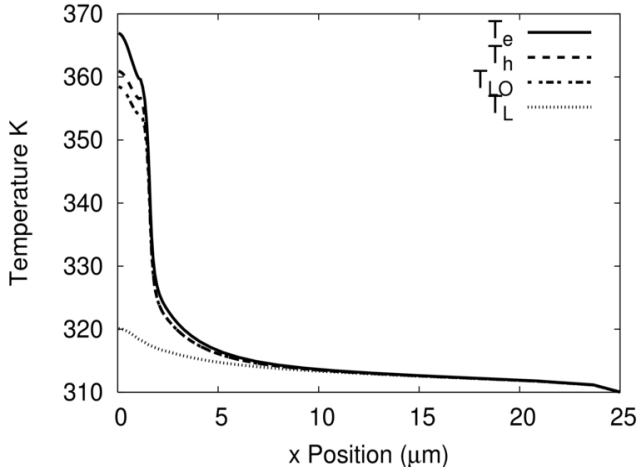

Figure 20: Lateral thermal profiles across the device obtained from a simulation neglecting TBR.

In this section, the impact of the thermal boundary resistance on the performance of a high-power 980nm ridge waveguide laser has been studied. It is found that with the inclusion of TBR, an increase in the QW lattice temperature of up to 0.4K is observed. This results in a decrease in the optical power of up to 0.6mW. Whilst the impact of TBR is still relatively small in the device considered here, its effects are somewhat greater than those found in smaller and lower power devices.

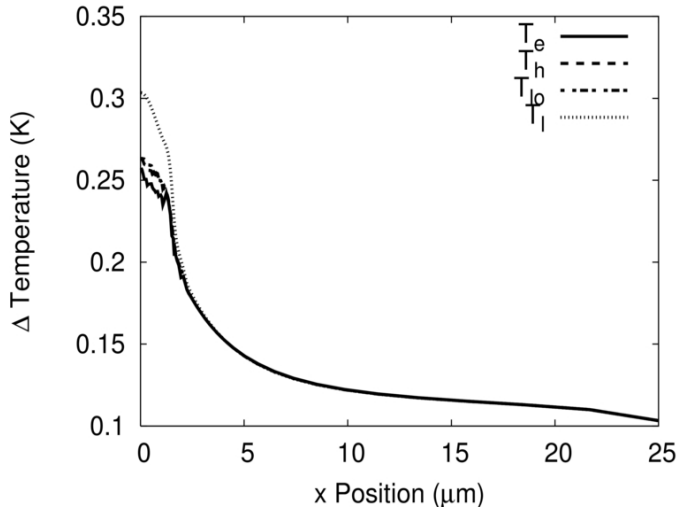

Figure 8.21: The differences in the thermal profiles caused by including TBR. At an injection current of 1.4A.

8.10 Carrier heat flux and TBR

8.10.1 Introduction

So far in this work, only the lattice heat flux has been taken into account. The heat transported by the carriers has been neglected. In order to fully consider the impact TBR has on a device, Possion's equation, the current continuity equation and the lattice heat flux equation must be solved self consistently along *with the carrier energy balance equations*. These two extra equations enable the electron and hole populations to have independent temperatures to that of the lattice. They introduce a three level bulk temperature model, where heat energy can be transported within the carrier populations via heat diffusion and electrical current flow. By including the carrier heat flux equations within the device simulator, it will be demonstrated that the carrier populations can absorb heat on one side of the TBR and deposit it on the other, thereby reducing the impact of the TBR. The derivation of the carrier energy balance

equations has been discussed in Chapter 5 and a derivation is available in Appendix A. For a more in depth treatment, the reader is referred to the doctoral dissertation of Martin Knaipp (1998) available from the Technical University of Vienna [31]. In the remainder of the chapter, the thermal model is extended to solve the carrier energy balance equations.

8.10.2 The model

The carrier energy balance equations are written in terms of an error (or remainder) function *f* for solution by Newton's method. The remainder of the carrier conservation equation for electrons is given as

$$f_n = \nabla\left(\frac{E_c}{q} - \phi\right)\cdot \boldsymbol{J_n} - \frac{3k_B}{2}\cdot\left(RT_n + n\frac{T_n - T_L}{\tau_n}\right) - \nabla\cdot\boldsymbol{S_n} \quad , \tag{8.90}$$

where f_n is the residual for the electron energy flux equation. Similarly, the residual of the hole heat flux equation f_h is written as

$$f_h = \nabla\left(\frac{E_c}{q} - \phi\right)\cdot \boldsymbol{J_h} - \frac{3k_B}{2}\cdot\left(RT_h + p\frac{T_h - T_L}{\tau_h}\right) - \nabla\cdot\boldsymbol{S_h} \quad . \tag{8.91}$$

The remainder of the lattice heat equation is

$$f_l = \nabla\cdot\kappa_L\nabla T_L + H \quad . \tag{8.92}$$

The electron heat flux is given as

$$\boldsymbol{S_n} = -\kappa_n\nabla T_n - \frac{5}{2}\frac{k_B T_n}{q}\boldsymbol{J_n} \tag{8.93}$$

and the hole heat flux is given as

$$\boldsymbol{S_p} = -\kappa_p \nabla T_p + \frac{5}{2}\frac{k_B T_p}{q}\boldsymbol{J_p} \quad . \tag{8.94}$$

The thermal conductivities of the carrier gasses are given by [33]

$$\kappa_n = \left(\frac{5}{2} + c_n\right)\frac{k_B^2}{q} T_n \mu_n n \tag{8.95}$$

$$\text{and} \quad \kappa_p = \left(\frac{5}{2} + c_p\right)\frac{k_B^2}{q} T_p \mu_p p \quad . \tag{8.96}$$

The lattice heating term is then given as

$$H = \frac{3k_B}{2}\cdot\left(n\frac{T_n - T_L}{\tau_n} + p\frac{T_p - T_L}{\tau_p}\right) + R(E_c - E_v + \frac{3}{2}k(T_e + T_h)) \tag{8.97}$$

8.10.3 Newton's method

The above equations are a set of highly non-linear differential equations. One of the most efficient solution methods is to use Newton's method. A simplified representation of the sparse matrix is

$$\begin{bmatrix} \frac{\partial f_l}{\partial T_l} & \frac{\partial f_l}{\partial T_e} & \frac{\partial f_l}{\partial T_h} \\ \frac{\partial f_e}{\partial T_l} & \frac{\partial f_e}{\partial T_e} & \frac{\partial f_e}{\partial T_h} \\ \frac{\partial f_h}{\partial T_l} & \frac{\partial f_h}{\partial T_e} & \frac{\partial f_h}{\partial T_h} \end{bmatrix} \begin{bmatrix} \Delta T_l \\ \Delta T_e \\ \Delta T_h \end{bmatrix} = - \begin{bmatrix} f_l \\ f_e \\ f_h \end{bmatrix} \tag{8.98}$$

Matrix (8.98) is solved for the update temperature vector [ΔT]. The temperatures are then updated as follows:

$$T_l^{k+1} = T_l^k + \Delta T_l^{k+1} \tag{8.99}$$

$$T_e^{k+1} = T_e^k + \Delta T_e^{k+1} \tag{8.100}$$

$$T_h^{k+1} = T_h^k + \Delta T_h^{k+1} \tag{8.101}$$

A sparse matrix solver written by the Numerical Algorithms Group [34-35] was used to solve the matrix. The carrier thermal conductivities were not included in the Newton solver. Instead, they were updated every iteration.

8.10.4 Jacobian elements

In order to solve 8.98, the derivatives must be calculated. Generally numerical derivatives are not accurate enough. Therefore analytical derivatives are used. These are given below:

Derivatives of the lattice heat conservation equation

$$\frac{\partial f_l}{\partial T_l} = \frac{\partial}{\partial T_l}\left(\nabla \cdot \kappa_L \nabla T_L\right) - \frac{3 k_B}{2} \cdot \left(\frac{n}{\tau_n} + \frac{p}{\tau_p}\right) \tag{8.102}$$

$$\frac{\partial f_l}{\partial T_e} = \frac{3 k_B}{2} \frac{n}{\tau_n} + \frac{3}{2} k R \tag{8.103}$$

$$\frac{\partial f_l}{\partial T_h} = \frac{3 k_B}{2} \frac{p}{\tau_p} + \frac{3}{2} k R \tag{8.104}$$

Derivatives of the electron heat conservation equation

$$\frac{\partial f_e}{\partial T_l} = \frac{3 k_B}{2}\left(\frac{-n}{\tau_n}\right) \tag{8.105}$$

$$\frac{\partial f_e}{\partial T_e} = \frac{3 k_B}{2}\left(R + \frac{n}{\tau_n}\right) - \frac{\partial}{\partial T_e} \nabla \cdot \boldsymbol{S_n} \tag{8.106}$$

$$\frac{\partial f_e}{\partial T_h} = 0 \tag{8.107}$$

Derivatives of the hole heat conservation equation

$$\frac{\partial f_h}{\partial T_l} = \frac{3k_B}{2}\frac{-p}{\tau_h} \tag{8.108}$$

$$\frac{\partial f_h}{\partial T_e} = 0 \tag{8.109}$$

$$\frac{\partial f_h}{\partial T_h} = -\frac{3k_B}{2}\left(R + \frac{p}{\tau_h}\right) - \frac{\partial}{\partial T_h}\nabla \cdot \boldsymbol{S_h} \tag{8.110}$$

8.10.5 Carrier relaxation times

To calculate the carrier relaxation times τ_e and τ_p, an empirical model based on Monte-Carlo simulation is implemented. In this model, the scattering time is a function of both the lattice and electron temperatures [36-38]. This model is applicable to all zinc-blende materials [36-38]. The scattering time for ternary alloys is given in terms of the scattering time for binary alloys using the following relation

$$\tau_{\epsilon,0}^{AB} = \tau_{\epsilon,0}^{A}(1-x) + \tau_{\epsilon,0}^{B}x + \tau_C(1-x)x \quad , \tag{8.111}$$

where the bowing parameter τ_C is given by

$$\tau_C = \tau_{\epsilon,0} + \tau_{\epsilon,1}\exp\left(C_1\left(\frac{T_n}{300} + C_0\right)^2 + C_2\left(\frac{T_n}{300} + C_0\right) + C_3\left(\frac{T_L}{300}\right)\right) \tag{8.112}$$

and

$$C_{\epsilon,0}^{AB} = C_{\epsilon,0}^{A}(1-x) + C_{\epsilon,0}^{B}x + C_C(1-x)x \quad . \tag{8.113}$$

The constants for AlGaAs are given in Table 8.3. A constant relaxation time of 0.1ps is used for the hole relaxation [36-38].

Material	τ_C[ps]	$\tau_{\varepsilon,1}$[ps]	C	C_1	C_2	C_3	$C^0{}_A$	$C_0{}^B$	$\tau_C{}^A$[ps]	$\tau_C{}^A$[ps]
AlGaAs	-0.35	0.025	-61	-0.053	0.853	0.5	0	61	0.48	0.17

Table 8.3: Constants to calculate scattering times [36-38].

8.10.6 Results for a simple slab of GaAs with a layer of defects

In order to gain an understanding of the how the lattice and electron heat fluxes interact around a TBR, a simple example is first examined. A TBR is placed half way down a slab of GaAs. (This situation could arise due to defect formation arising from a regrowth step and a dirty interface.) Although TBRs are more commonly associated with the interface of two dissimilar materials, this example offers a way to examine the interaction the carrier/lattice heat fluxes around a TBR without the added complication of a change in the band structure which introduces additional heating terms and makes the interpretation of the results more difficult.

The slab is doped with $1x10^{23}m^{-3}$ donors. Each end of the slab is capped with a thin layer of gold, so that the electron and lattice temperatures are assumed to be in equilibrium at both ends of the slab, i.e.

$$T_l(0)=T_e(0)=T_h(0) \quad T_l(L)=T_e(L)=T_h(L) \quad . \tag{8.114}$$

A voltage is applied across the device and the interplay of electron heat, lattice heat and TBR are examined. The electron and lattice temperatures across the device are plotted in figure 8.22. A clear step in the middle of the graph is visible for both the electron and lattice temperatures due to the TBR. The step in the lattice temperature is very abrupt due to phonon reflections at the interface. However, the step in the electron temperature is much smoother, because of the finite time it takes electrons to

lose energy to the lattice.

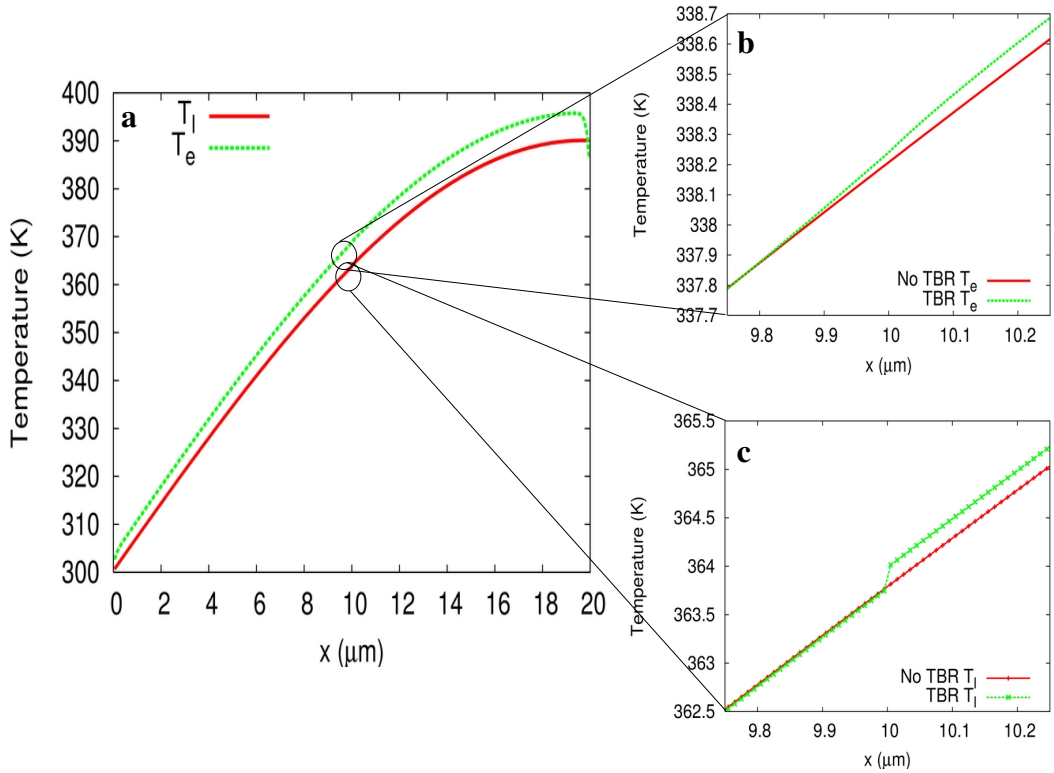

Figure 8.22: (a) Thermal distribution across the device, (b) zoomed in section of electron thermal profile and (c) zoomed in section of the lattice thermal profile. The impact of the TBR is clearly seen, as a discrete step in temperature. The electron temperature can be seen relaxing slowly over the interface.

The rate at which electrons lose energy to the lattice is plotted in figure 8.23. The overall shape of the curve is due to the T_n-T_l term in (8.90). The presence of the double spike over the TBR can be explained by the abrupt change in lattice temperature and the gradual change in electron temperature. On the up stream side of the TBR, the electron temperature starts to approach the lattice temperature, so that the electron relaxation rate decreases. This can be thought of as energy being given to the carriers from the lattice. As soon as the TBR is reached, there is a sudden drop of

the lattice temperature away from the electron temperature. Thus, the energy loss rate of the electrons suddenly increases, so that the energy transferred to the carriers from the up stream side of the TBR is returned to the lattice.

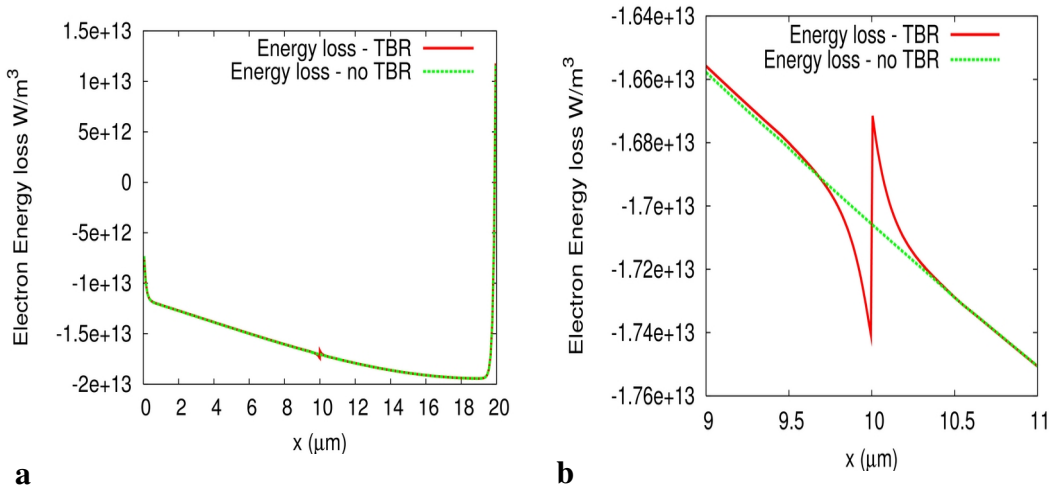

Figure 8.23: (a) Electron relaxation rate over the whole device, (b) zoomed in section over TBR.

In figure 8.24, the two heat fluxes for the lattice S_l and for the electron population S_e are plotted. Note that the lattice heat flux is greater than that of the electron energy flux by an order of magnitude. Note also that the energy fluxes on the right hand side of the graph both tend to zero. This is because of the isothermal boundary condition assumed on the right hand side of the simulation. The general shape of the electron energy flux is determined by the term JT_e in the energy flux equation 8.93 and has the biggest effect on determining the shape and magnitude of the curve. The double hump in the centre of the graph is produced by the ∇T_e term as the electron temperature rapidly decreases over the TBR.

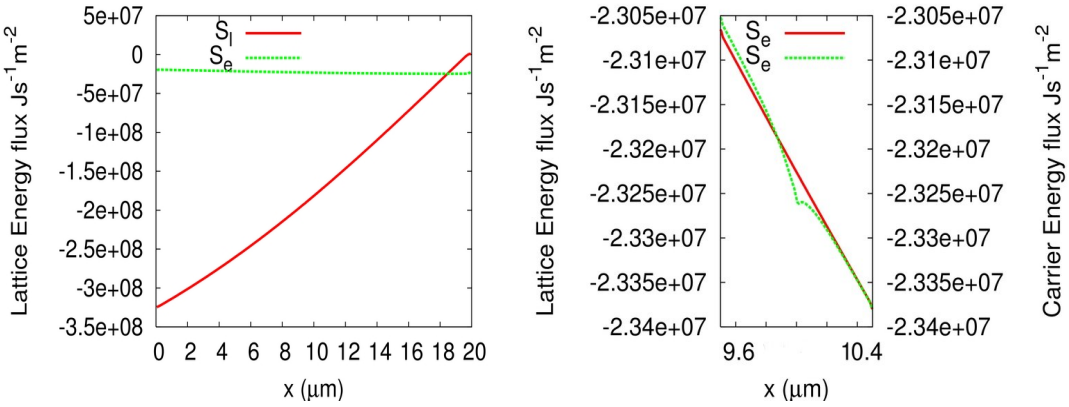

Figure 8.24: Energy fluxes across the device, with TBR included in the simulation.

8.10.7 Summary and further work on the transfer of heat due to carriers over thermal boundary resistances

In this subsection, the interaction of electron and lattice heat flux over a TBR has been examined. It has been found, through a simple example, that the electron heat flux can reduce the impact of a TBR over an interface. Further work in this area was limited by the stability of the model. Indeed, hydrodynamic models are well known for their instability. The main cause of this instability arises from areas of low carrier concentration. In these areas, carrier relaxation rates and heat conduction are very low. It therefore requires a very small error in the solution to start producing very large temperatures in these areas. Once these are fed back into the electrical model, they can cause it to diverge from the correct solution. There are solutions available [40], but they are outside of the scope of this work. If this area were to be examined further, a more robust model should be built.

8.11 Summary - Overview

In this chapter, the concept of thermal boundary resistance has been introduced. The methods available for calculating values of TBR have been reviewed and a finite-difference scheme has been adapted from electromagnetics to introduce a step-wise gradient change in the temperature profile at material interfaces. The scheme has been incorporated into a state-of-the-art device simulator.

8.11.1 Summary - Edge emitting lasers

The impact of thermal boundary resistance on the performance of a high-power 980nm ridge waveguide laser has been studied. It is found that an increase in the QW lattice temperature of up to 0.4K is observed with the inclusion of TBR. This results in a 0.6mW decrease in optical power. Whilst the impact of TBR is relatively small in the devices considered here, its effects are somewhat greater than those found in the 1.3μm low power devices. This suggests that the effects of TBR could be more significant in structures operating at higher powers.

8.11.2 Summary - VCSELs

It is well known that the VCSELs have a much lower thermal conductivity than would be predicted from the bulk thermal conductivity values alone [39]. The example in this chapter demonstrated the dual impact of TBR on such a structure - the increase in temperature caused by the TBR itself and the reduction in bulk thermal conductivity caused by the increased temperature. It also suggests that the effect could be

important in edge emitting devices with short period superlattice (SPSL) cladding layers.

8.11.3 Summary – Carrier/lattice heat flux

The full set of hydrodynamic equations has been solved and it has been shown that carrier heat fluxes can reduce the impact of TBR because of the parallel heat transport mechanism across the interface.

8.11.4 Concluding remarks and further work

1. Currently, a truly predictive and accurate model for calculating the value of TBR is not available.
2. There is a lack of a systematic study of the TBRs associated with the materials found in optoelectronic devices.
3. Both a macroscopic model and experimental values that agree are needed before TBR can be included in optoelectronic device simulators in a useful way.
4. As the size of devices shrinks to the nanometer (e.g. QCLs) scale, the need for accurate and predictive models for TBR will become increasingly important.

8.12 References

[1] G. K. Wachutka, "Rigorous Thermodynamic Treatment of Heat Generation and Conduction in Semiconductor Device Modeling", IEEE Transactions on

computeraided design", 9, 11, pp. 1141-1149, 1990

[2] G. K. Wachutka, "Rigorous Thermodynamic Treatment of Heat Generation and Conduction in Semiconductor Device Modeling", IEEE Transactions on computeraided design", 9, 11, pp. 1141-1149, 1990

[3] G.Wachutka, "Unified framework for thermal, electrical, magnetic, and optical semiconductor device modeling", COMPEL, 10, pp. 311-321, 2004

[4] S. Rudin, G. Wachutka and H Baltes, "Thermal Effects in Magnetic Microsensor Modeling", Sensors and Actuators A. pp.731-735, 1991

[5] M. Lundstorm, "Fundamentals of carrier transport - Second Edition", Cambridge University Press, ISBN:0521631343, 2000

[6] J. Piprek, "Semiconductor Optoelectronic Devices Introduction to Physics and Simulation", Academic Press ,ISBN 0387226591, 2005

[7] M. Knaipp, "Modellierung von Temperatureinflüssen in Halbleiterbauelementen", Dissertation - Technische Universität Wien Fakultät für Elektrotechnik , September 1998

[8] E.M. Azoff, "Generalized energy-momentum conservation equations in the relaxation time approximation", Solid-State Electron., 30, 9, pp. 913-917, 1987.

[9] P.L. Kapitza, "The study of heat transfer in helium II", Zh. Eksp. Teor. Fiz. 11, 1, 1941 [J. Phys. (USSR) 4, 181], 1941

[10] E.T Swartz and R.O. Pohl, "Thermal boundary resistance", Reviews of Modern Physics, 61, 3, 1989

[11] K.A. Filippov and A.A. Balandin, MRS Internet J. Nitride Semiconductor Research, 8, 2003

[12] T. A. Eckhause, Ö. Süzer, Ç. Kurdak, F. Yun and H. Morkoç, "Electric-field-induced heating and energy relaxation in GaN", Appl. Phys. Lett., 82, 3035, 2003

[13] W.S. Capinski, H.J. Maris, T. Ruf, M. Cardona, K. Ploog and D.S. Katzer, "Thermal-conductivity measurements of GaAs/AlAs superlattices using a picosecond optical pump-and-probe technique ", Phys. Rev. B, 59, pp. 8105-8113, 1999

[14] G. Chen, "Phonon heat conduction in nanostr",International Journal of Thermal Sciences , 39, pp. 471-480, 2000

[15] B.A. Auld, "Acoustic fields and waves in solids", Volume 1, R.E. Krieger, ISBN 089874783X, 1990

[16] Daly et al., "Molecular dynamics calculation of the thermal conductivity of superlattices", Phys. Rev. B, 66, pp. 024301, 2002

[17] W.S. Capinski, H.J. Maris, T. Ruf, M. Cardona, K. Ploog and D.S. Katzer, "Thermal-conductivity measurements of GaAs/AlAs superlattices using a picosecond optical pump-and-probe technique", Phys. Rev. B, 59, 8105, 1999

[18] G. Chen, "Phonon heat conduction in nanostr",International Journal of Thermal Sciences , 39, pp. 471-480, 2000

[19]W.A. Little, "The transport of heat between dissimilar solids at low temperatures", Canadian Journal of physics, 37, , pp. 334-349, 1959.

[20] R. Stevens et.al. "Molecular-Dynamics study of thermal boundary resistance: Evidence of strong inelastic scattering transport channels", Proc. of IMECE04 2004 ASME Int. Mechanical Engineering Congress of IMECE04 November 13-20, Anaheim, California USA 2004, 2004

[21] Swartz, E.T. et al. , 1987, "Thermal resistance at interfaces" App. Phys. Lett., 51,

pp. 2200-2202

[22] A. Sergeev, "Inelastic electron-boundary scattering in thin films", Physica B Physics of Condensed Matter, 263, p. 217-219, 1999

[23] A.V. Sergeev, "Electronic Kapitza conductance due to inelastic electron-boundary scattering", Phys. Rev. B, 58, R10199 - R10202, 1998

[24] E.T Swartz, R.O. Pohl, "Thermal boundary resistance", Reviews of Modern Physics, 61, 3, pp.621, 1989

[25] G. Scamarcio, M.S. Vitiello, V. Spagnolo and A. Lops, "Thermal and electronic analysis of GaInAs/AlInAs mid-IR QCLs", Phonons Paris, 2007

[26] J. Kuzmík, S. Bychikhin, D. Pogany and C. Gaquière, "Investigation of the thermal boundary resistance at the III-Nitride/substrate interface using optical methods", J. Appl. Phys., 101, 054508, 2007

[27] M.S. Stern, "Semivectorial polarised finite difference method for optical waveguides with arbitrary index profiles", IEE Proceedings, 135, 1, pp. 56-63, 1998

[28] IOFFE on-line materials data base of material constnats, http://www.ioffe.rssi.ru/SVA/NSM/, acceseed 15 Feb 2008

[29] N. Lichtenstein et al., "DPSSL and FL Pump Based on 980nm-Telecom Pump Laser Technology: Changin the Industry", 2nd Conference on high-power diode laser technology an applications, Proc. Of SPIE, 5336, pp.77-83, 2004

[30] Rodriguez D., "Measurement of gain spectra, refractive index shift and line width enhancement factor in Al-free 980nm lasers with broadened waveguide", SPIE, 4646, pp. 344-354, 2002

[31] M. Knaipp, "Modellierung von Temperatureinflüssen in

Halbleiterbauelementen", Technischen Universität Wien, September 1998 English: "Moderling of temperature effects in semiconductor devices", Technical University of Viena September 1998

[32] Yang Liu et al., "Numerical investigation of self-heating effects of oxide-confined vertical-cavity surface-emitting lasers", J. Quant. Electron. 41, 1, pp.15- 25, 2005

[33] S. Selberherr "Analysis and Simulation of Semiconductor Devices", ISBN:3211818006,1984

[34] Numerical Algorithms Group Manual, Mark 21, routine: f11dcf

[35] Numerical Algorithms Group Manual, Mark 21, routine: f01brf and f04axf.

[36] B. Gonzalez, V. Palankovskib, H. Kosinab, A. Hernandeza and S. Selberherrb ,"An energy relaxation time model for device simulation", Solid-State Electron., 43, pp. 1791-1795, 1999

[37] Vassil Palankovski, "Dissertation: Simulation of Heterojunction Bipolar Transistors", Dezember 2000 Wien, Österreich http://www.iue.tuwien.ac.at/phd/palankovski/node51.html, accessed: 15 Feb 2008

[38] S. Selberherr, "Analysis and Simulation of Semiconductor Devices - Computational Microelectronics", Springer, ISBN 3211818006, p. 112, 1984

[39] C. W. Wilmsen, H. Temkin and L. A. Coldren "Sertical-Cavity Surface-Emitting Lasers: Design, Fabrication, Characterization and Applications", Cambridge University Press, ISBN 0521006295, 1999

[40] M. Grupen, Private communication, 2007